ARTICLE INFO
Article ID: 10-11-01-0008
© 2027 Jifeng Wang, Penghu Li, Jie Yan, Liang Zhang, Hongwei Yi, Yuwei Deng, Haibo Huang
doi:10.4271/10-11-01-0008

Vehicle Wind Noise Prediction Based on Wasserstein Generative Adversarial Network and Squeeze-and-Excitation Xception Network

Jifeng Wang,[1] Penghu Li,[1] Jie Yan,[1] Liang Zhang,[2] Hongwei Yi,[3] Yuwei Deng,[4] and Haibo Huang[1]

[1]*Southwest Jiaotong University, China*
[2]*CATARC: China Automotive Technology and Research Center, China*
[3]*Xihua University, China*
[4]*China FAW Group Corporation R and D Center: First Automobile Works Group Corporation Research and Development Center, China*

Abstract

To address the challenge of efficiently evaluating vehicle aeroacoustic characteristics during the preliminary modeling stages, this article proposes an interior wind noise prediction method based on styling features and the squeeze-and-excitation module and Xception network. Drawing upon wind tunnel test data from sport utility vehicles of various dimensions operating under a 120 km/h condition, key styling parameters were identified based on vehicle geometry. Furthermore, to overcome the limitations associated with small sample sizes, a Wasserstein generative adversarial network is introduced to augment the original wind noise dataset. Subsequently, a complex nonlinear correlation is established between the acquired geometric parameters and the interior wind noise level. Validation results demonstrate that the proposed model achieved average MAPE values of 3.18%, 3.75%, and 3.26%, along with average RMSE values of 1.12 dB, 1.20 dB, and 1.19 dB, respectively, across three independent validation vehicles, indicating its promising efficiency and accuracy for vehicle wind noise evaluation. This research provides a streamlined and robust methodology to expedite the evaluation of interior wind noise, offering a practical technical reference for aerodynamic noise control during the preliminary styling stages.

History

Received: 03 Jul 2026
Revised: 26 Aug 2026
Accepted: 14 Oct 2026
e-Available: 05 Nov 2026

Keywords

Interior wind noise, Squeeze-and-Excitation module, Xception, Small dataset, Wasserstein generative adversarial network

Citation

Wang, J., Li, P., Yan, J. Zhang, L., et al., "Vehicle Wind Noise Prediction Based on Wasserstein Generative Adversarial Network and Squeeze-and-Excitation Xception Network," *SAE Int. J. Veh. Dyn., Stab., and NVH* 11(1):2027, doi:10.4271/10-11-01-0008.

ISSN: 2380-2162
e-ISSN: 2380-2170

© 2027 Jifeng Wang, Penghu Li, Jie Yan, Liang Zhang, Hongwei Yi, Yuwei Deng, Haibo Huang. Published by SAE International. This Open Access article is published under the terms of the Creative Commons Attribution License (http://creativecommons.org/licenses/by/4.0/), which permits distribution, and reproduction in any medium, provided that the original author(s) and the source are credited.



1. Introduction

Driven by ongoing advancements in the vehicular sector, buyer demands regarding holistic automotive capabilities are shifting from mere powertrain output and fuel efficiency to more refined experiential metrics, notably ride smoothness and interior acoustic comfort [1, 2]. Given its decisive role in occupant comfort, in-cabin acoustic behavior has drawn heightened focus across both academic investigations and industrial applications. The sources of interior noise are diverse, primarily encompassing powertrain noise [3, 4], tire–road interaction noise [5–7], and aerodynamic noise [8, 9]. Studies indicate that at vehicle speeds exceeding 100 km/h, the energy contribution of aerodynamic noise within the mid-to-high-frequency band (800–5000 Hz) can constitute more than three-fifths of the overall in-cabin acoustic energy [10, 11]. Furthermore, the advancement of vehicle electrification has led to a significant reduction in powertrain noise [12, 13], thereby amplifying the prominence of aerodynamic noise [14, 15]. Research indicates that elevated interior noise levels not only adversely affect the physical and psychological well-being of drivers [16, 17] but can also cause distraction, thereby escalating traffic safety risks [18]. Concurrently, zones of intense acoustic emission are typically coupled with severe turbulent wake structures and amplified wind resistance, which in turn exacerbate the power expenditure of battery-powered automobiles [19]. Consequently, managing high-frequency aeroacoustic sources prior to physical prototyping represents a crucial technical task aimed at optimizing the entire automobile's interior comfort and general energy utilization.

The evaluation of automotive wind noise performance is primarily conducted through wind tunnel testing [20, 21]. In related research, Staron et al. [22] investigated full-vehicle wind noise under unsteady crosswind conditions utilizing an aeroacoustic wind tunnel. By employing synchronized measurements from microphone arrays and surface pressure sensors, they analyzed the impact of crosswinds on aerodynamic noise in the A-pillar and rearview mirror regions, demonstrating that complex inflow conditions significantly amplify local broadband noise. Similarly, Jamaluddin et al. [23] investigated modulated interior wind noise under transient airflow conditions using an active crosswind apparatus in Germany. Through synchronized measurements of microphone arrays and side window surface pressure, they analyzed the characteristics of interior wind noise under dynamic crosswind conditions and its correlation with transient flow fields, also concluding that complex inflows significantly intensify interior broadband noise. Furthermore, Zhang et al. [24] combined full-scale wind tunnel testing with large eddy simulation to identify and analyze aerodynamic sound sources on the exterior surface of a sport utility vehicle (SUV). Their study revealed that the A-pillar, rearview mirrors, and front wheel regions are the primary distribution areas for dipole sound sources, contributing to over 80% of the total acoustic energy on the vehicle exterior. While wind tunnel testing, as a traditional wind noise analysis method, can accurately capture vehicle wind noise levels, it is hindered by high experimental costs and prolonged testing cycles, thereby precluding the feasibility of rapid iterative analysis.

To circumvent the intrinsic constraints of traditional wind tunnel testing in capturing complex flow fields and accommodating protracted development cycles, computational fluid dynamics has emerged as an essential auxiliary tool for automotive wind noise research [25, 26]. Josefsson et al. [27] investigated the external flow field structures of SUVs utilizing high-resolution numerical simulations and wind tunnel experiments. Their findings indicate that vortex structures in the wake and wheel regions are strongly correlated with surface pressure fluctuations, significantly impacting vehicle aerodynamic drag and aerodynamic noise under high-speed conditions. Nomani et al. [28] proposed a simulation-based identification method to analyze the aerodynamic noise of rooftop air-conditioning systems in commercial vehicles, effectively mitigating airborne noise by optimizing local separated flow structures. Employing this methodology, Sharma et al. [29] conducted aeroacoustic research on commercial vehicle styling. By comparatively analyzing noise transmission characteristics inside and outside the cabin through wind tunnel tests and numerical simulations, they validated the coupling relationship between complex external flow field structures and interior wind noise. Alwadei et al. [30] introduced a high-fidelity aeroacoustic prediction method based on the coupling of large eddy simulation and vibro-acoustics. This approach realized the numerical simulation of the transmission process from external flow field pressure fluctuations to interior noise, confirming the method's efficacy in predicting mid-to-high-frequency wind noise. While computational fluid dynamics (CFD) methods provide detailed insights into aerodynamic flow structures and allow flexible adjustments of vehicle configurations, operating conditions, and boundary parameters, their practical application in the early vehicle development stage remains constrained by high computational costs and long simulation cycles [31]. Particularly, when numerous styling iterations and optimization schemes need to be evaluated within a limited development period, the substantial computational resources required by high-fidelity CFD simulations may hinder rapid design exploration and decision-making.

Recently, machine learning algorithms and data-centric frameworks have gained significant traction within the domain of in-cabin acoustic suppression [32, 33]. Machine learning algorithms are leveraged to uncover

the intricate higher-order interdependencies linking acoustic signatures to automotive design variables. This not only significantly enhances the accuracy of noise prediction models but also substantially shortens the development cycle for overall vehicle acoustic performance. The physics-informed neural networks introduced by Raissi et al. [34] in 2019 embedded governing differential formulations as physical regularizers during the optimization phase, substituting physical laws for massive datasets and demonstrating unique advantages in data-scarce engineering scenarios. Furthermore, Roznowicz et al. [35] proposed a surrogate model for large-scale three-dimensional external flow fields based on graph neural networks. By learning spatial correlation features within complex external flow fields, this method realized the rapid prediction of vehicle exterior aerodynamic flow fields. Compared to traditional CFD, its computational efficiency is markedly improved while accurately reconstructing pressure and velocity distributions. Nevertheless, data-driven algorithms exhibit a strong dependency on sample scale [36]. In practical engineering applications, constrained by factors such as cost and computational capacity, valid automotive wind noise data is frequently limited. This scarcity yields insufficient sample data for model training, rendering the models susceptible to underfitting or diminished accuracy.

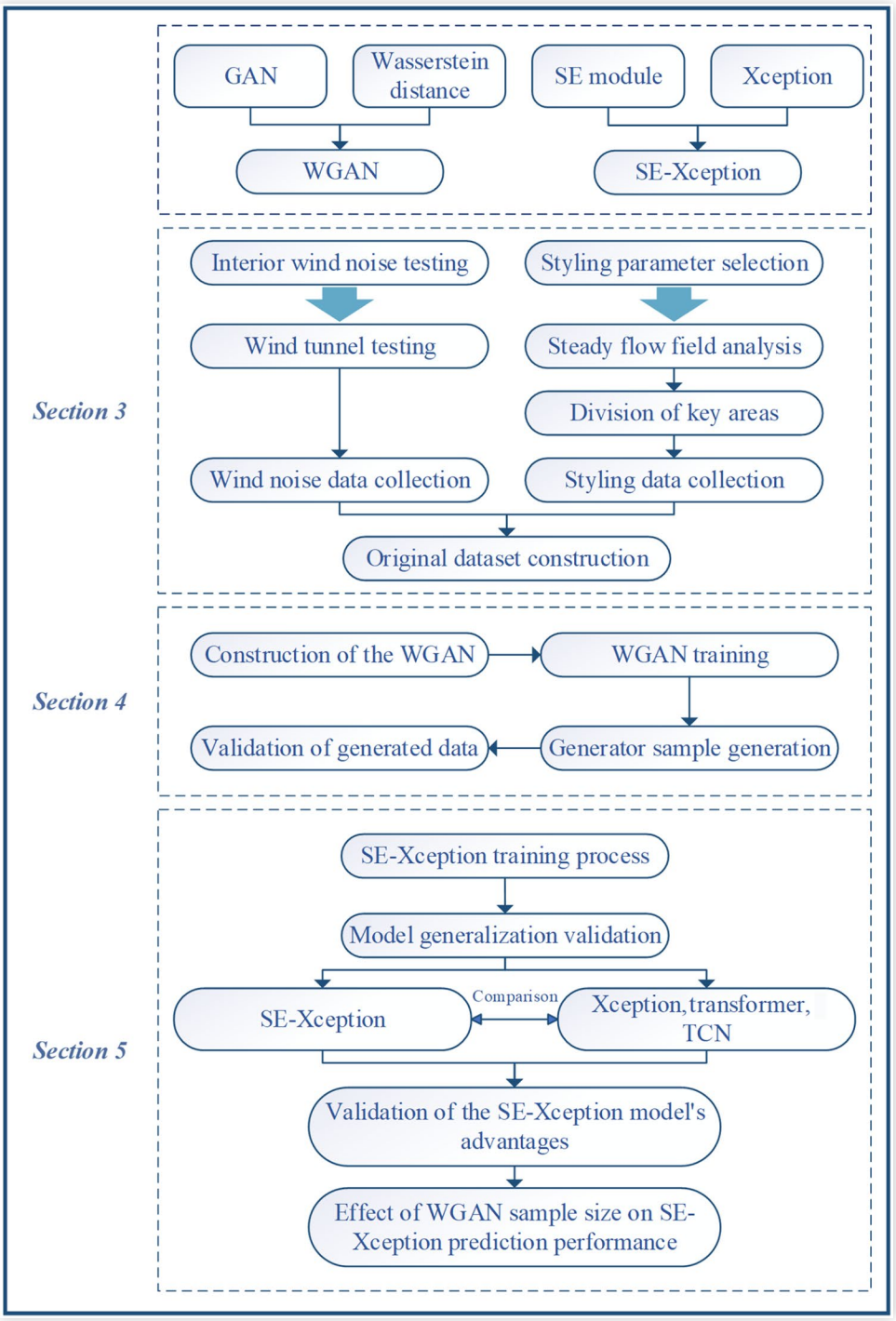
However, existing machine learning approaches still face several challenges in the field of automotive aeroacoustics. First, previous studies have primarily focused on the prediction of external aerodynamic performance, flow field characteristics, and aerodynamic forces, whereas investigations into the interior wind noise response at the driver's perceptual location remain relatively limited. In particular, the direct mapping relationship between vehicle styling parameters and frequency-dependent acoustic characteristics has not been sufficiently explored. This is mainly because interior wind noise is jointly influenced by multiple factors, including vehicle geometry, local flow structures, and acoustic transmission paths, resulting in a highly nonlinear and complex prediction problem. Second, existing data-driven models generally require a large amount of experimental data or high-fidelity simulation data for model training. However, in practical vehicle development processes, the acquisition of aeroacoustic data is often associated with considerable costs. This challenge becomes more prominent during the conceptual design stage, where complete vehicle models and sufficient wind noise samples may not yet be available. Consequently, the applicability of data-driven methods in early stage vehicle design remains constrained.

Building upon the preceding analysis, this article presents two primary technical contributions for the effective prediction of automotive wind noise:

1. Conventional wind noise evaluation methods generally rely on complete digital vehicle models, computationally intensive aeroacoustic simulations, or physical vehicle testing, making them difficult to apply efficiently during the initial design stage. Therefore, this study proposes a vehicle styling geometry parameter-driven method for interior wind noise prediction at the early styling design stage. By establishing a nonlinear mapping between vehicle styling parameters, acoustic transfer characteristics, and the wind noise response at the driver's outer-ear position, the proposed method enables rapid prediction of interior wind noise without requiring a complete vehicle model. On this basis, the Squeeze-and-Excitation (SE) attention mechanism is incorporated into the Xception network to construct the SE-Xception model, enhancing its ability to integrate early stage styling parameters and capture diverse vehicle styling characteristics.
2. Since automotive wind noise testing requires complete physical vehicle prototypes and involves relatively high testing costs, it is difficult to obtain a sufficiently large dataset during the early stage of vehicle design. Therefore, this study employs a Wasserstein generative adversarial network (WGAN) to augment the limited automotive wind noise dataset and systematically investigates the effects of different augmentation scales on prediction performance. WGAN is employed to learn the underlying distribution characteristics of the original data and generate representative synthetic samples, thereby expanding the dataset and mitigating the risk of overfitting under limited-data conditions. Furthermore, the effects of different numbers of augmented samples and different numbers of original samples on prediction performance are systematically investigated. The resulting relationship between dataset size and prediction accuracy provides a basis for determining an appropriate augmentation scale and constructing wind noise prediction models under limited-data conditions.

Beyond the introductory remarks, Section 2 details the fundamental Xception network, the SE-Xception architecture integrating the channel attention mechanism, alongside the WGAN-based solution for small sample sizes. Section 3 details the acquisition process of interior wind noise data and the subsequent dataset construction. Section 4 elaborates on the configuration of the WGAN and analyzes the generated synthetic data. Section 5 presents the SE-Xception interior wind noise prediction model, evaluates its predictive performance and generalization capability, and examines the impact of the augmented sample size on the prediction outcomes. Finally, Section 6 summarizes the primary contributions and conclusions of this research. The overall technical workflow is shown in Figure 1.

FIGURE 1 Technical workflow.



© Jifeng Wang, Penghu Li, Jie Yan, Liang Zhang, Hongwei Yi, Yuwei Deng, Haibo Huang

2. The Proposed Method

2.1. Brief Introduction of Xception Network

As a variant of convolutional neural networks, the Xception model excels at extracting high-dimensional data features while optimizing computational complexity [37, 38]. Its core mechanism, depthwise separable convolution, effectively decouples the learning processes of spatial and channel features. This architectural design successfully circumvents the issues of parameter redundancy and excessive computational costs inherent in traditional standard convolutions.

The architectural blueprint of the Xception network is fundamentally structured around a tripartite cascade, sequentially comprising the entry, middle, and exit flows [39], as illustrated in Figure 2. The entry flow integrates a sequence of conventional convolution modules and strided depthwise separable convolution modules, primarily tasked with the initial feature extraction and spatial dimensionality reduction of the raw input data [40]. The middle flow comprises heavily repeated stacks of depthwise separable convolution modules [41, 42], functioning to refine features across multiple hierarchical levels. Subsequently, the exit flow incorporates downsampled depthwise separable convolution modules, accompanied by a global spatial mean-pooling block coupled with a dense projection unit, thereby mapping the features extracted from the middle flow into the output space to execute the target prediction.

2.2. Proposed SE-Xception Network

The SE module is a classic channel attention mechanism. By introducing adaptive weight learning along the channel dimension of convolutional neural networks, it enables the model to dynamically recalibrate the importance of each channel, thereby enhancing the expressive capability of the feature representations [43, 44]. The architecture of this module is illustrated in Figure 3.

The core workflow of the SE module is divided into three stages: squeeze, excitation, and recalibration [45]. The specific implementation of each operation is as follows.

Assuming the input feature map is $U \in \mathbb{R}^{W\times H\times C}$ (where W and H denote the spatial dimensions and C represents the number of channels), the SE module initially executes a spatial reduction across each channel, yielding a discrete scalar parameter by means of global average pooling, thereby generating a channel descriptor vector $Z \in \mathbb{R}^{C}$. For the feature map of the channel indexed by c, denoted as $u_c \in \mathbb{R}^{W\times H}$, this step can be expressed as Equation 1:

$$Z_c = F_{sq}\left(u_c\right) = \frac{1}{W\times H}\sum_{i=1}^{W}\sum_{j=1}^{H} u_c\left(i,j\right) \tag{1}$$

The excitation module initially compresses the number of channels to $\frac{C}{r}$ through a dimensionality-reduction fully connected layer (parameterized by $W_1 \in \mathbb{R}^{\frac{C}{r}\times C}$, where r represents the reduction ratio), subsequently introducing nonlinearity via a ReLU activation function $\delta(\cdot)$. Following this, the channel dimensions are restored by a dimensionality-increasing fully connected layer (parameterized by $W_2 \in \mathbb{R}^{C\times\frac{C}{r}}$) and normalized to the [0,1] interval using a Sigmoid function $\sigma(\cdot)$, ultimately yielding the channel weight vector S. This step can be expressed as Equation 2:

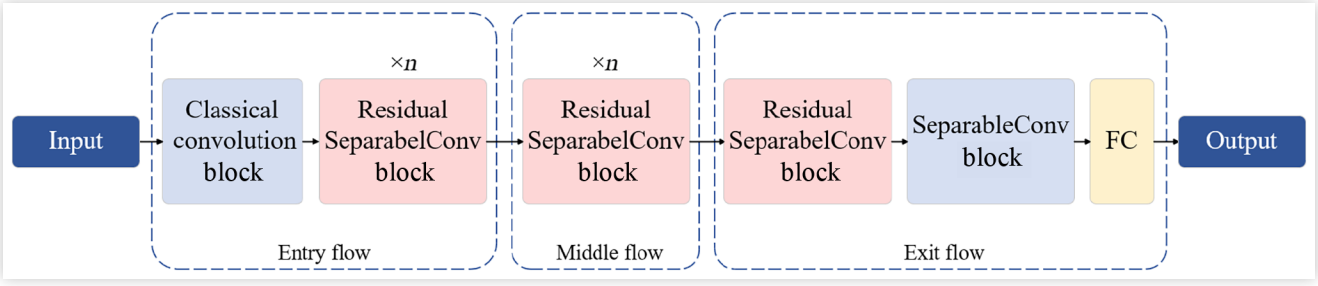
$$s = F_{ex}\left(Z,W\right) = \sigma\left(W_2\cdot\delta\left(W_1\cdot Z\right)\right) \tag{2}$$

where $W = \{W_1, W_2\}$ represent learnable parameters. This process facilitates the adaptive learning of the relative importance of each individual channel.

The recalibration operation entails channel-wise multiplication between the learned channel weights s and the original feature map U to achieve dynamic feature adjustment. This process can be expressed as Equation 3:

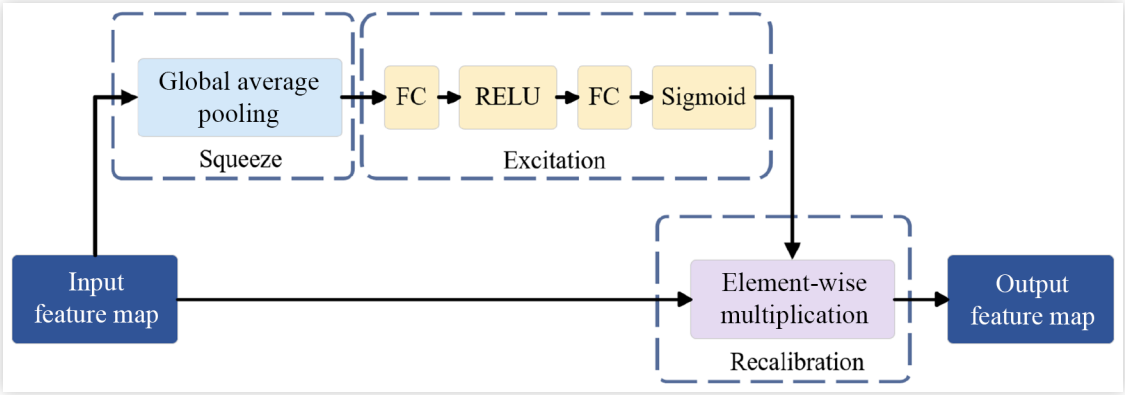
$$\tilde{X}_c = F_{scale}\left(u_c, s_c\right) = s_c\cdot u_c \tag{3}$$

FIGURE 2 Architecture of the Xception.



© Jifeng Wang, Penghu Li, Jie Yan, Liang Zhang, Hongwei Yi, Yuwei Deng, Haibo Huang

FIGURE 3 Architecture of the SE module.



© Jifeng Wang, Penghu Li, Jie Yan, Liang Zhang, Hongwei Yi, Yuwei Deng, Haibo Huang

where $\tilde{X}_c \in \mathbb{R}^{W\times H}$ denotes the recalibrated feature of the channel indexed by c and s_c represents the weight of the channel indexed by c. Through a "weighted enhancement-suppression" mechanism, this operation amplifies the feature responses of critical channels ($s_c \approx 1$) while attenuating the interference from redundant channels ($s_c \approx 0$), thereby elevating the model's representational capacity for relevant features.

While Xception leverages depthwise separable convolutions to decouple spatial and channel correlations, thereby drastically reducing computational complexity, its pointwise convolution for processing channel relationships fails to distinguish which channels contain more critical information. Therefore, this article introduces the SE module into the Xception network, enabling the model to learn inter-channel dependencies and endowing the extracted features with enhanced discriminative power [46]. From the perspective of aerodynamic noise generation, vehicle interior wind noise is induced by coupled effects of flow separation, vortex shedding, and unsteady pressure fluctuations around local geometric features. Different styling parameters contribute unequally to these aerodynamic phenomena and exhibit frequency-dependent impacts on acoustic responses. Conventional Xception treats feature channels equally after pointwise convolution, which limits its ability to distinguish critical aerodynamic–acoustic information. The SE module overcomes this limitation by adaptively recalibrating channel-wise feature responses, emphasizing informative features while suppressing irrelevant ones. Therefore, integrating SE into Xception enables the model to capture dominant aerodynamic–acoustic characteristics and learn the complex nonlinear relationship between vehicle styling parameters and interior wind noise. The specific architecture of the proposed SE-Xception network is illustrated in Figure 4.

2.3. Brief Introduction of GAN and WGAN

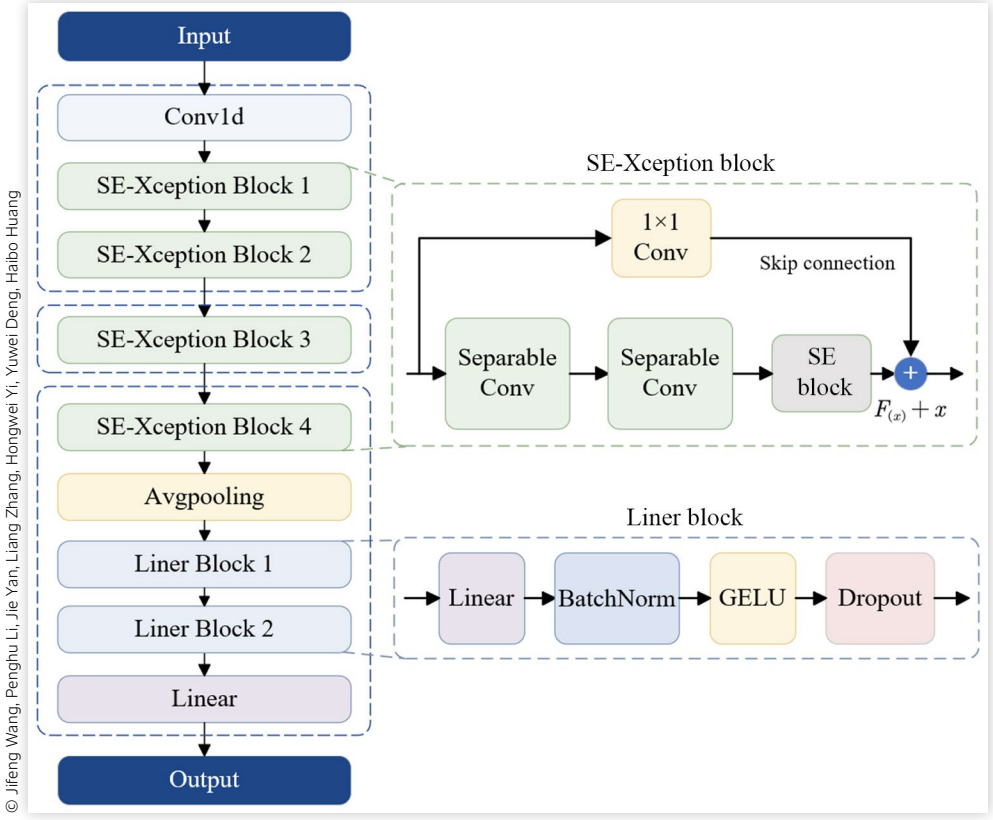
The core principle of a generative adversarial network (GAN) involves training two neural networks via an adversarial framework, thereby facilitating the learning and simulation of real data distributions [47, 48]. A typical GAN consists of a generator and a discriminator [49], and its fundamental architecture is illustrated in Figure 5.

During training, the generator endeavors to deceive the discriminator, rendering it incapable of distinguishing between real and synthetic data, while the discriminator strives to accurately differentiate authentic samples from generated ones. Through alternating optimization and mutual adversarial competition, the generator ultimately learns the true data distribution, reaching a state where the discriminator can no longer discern authenticity. The training process of the GAN can be formulated as Equation 4:

$$\min_G \max_D V(D,G) = \mathbb{E}_{x\sim p_{\text{data}}}\left[\log D(x)\right] + \mathbb{E}_{z\sim p_z}\left[\log\left(1-D\left(G(z)\right)\right)\right] \quad (4)$$

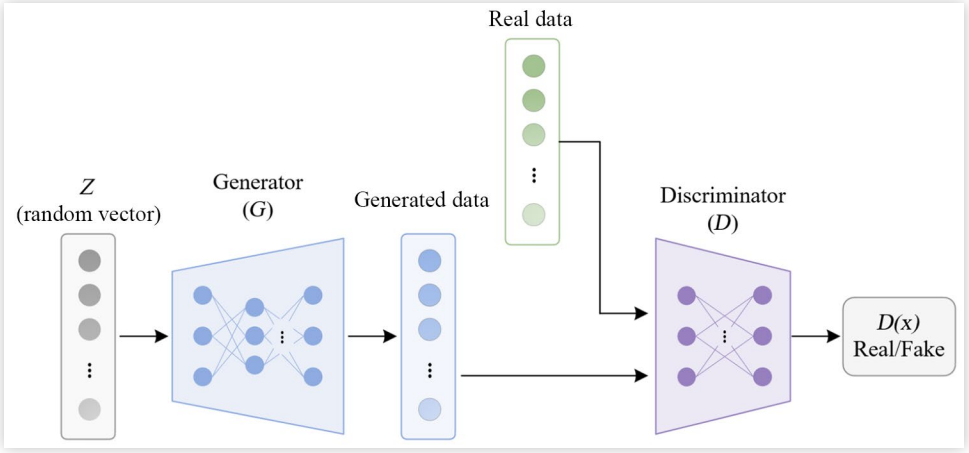
where x denotes the real data, z represents the input noise, $D(x)$ indicates the probability that the discriminator classifies x as a real sample, $G(z)$ is the fake sample generated from the noise by the generator, p_d characterizes the underlying real data distribution, and p_z denotes the predefined noise space. The GAN training process alternates between the discriminator and the generator. The discriminator learns the distinguishing features of real and fake data utilizing both authentic and synthetic samples, while the generator continuously optimizes its output based on feedback from the discriminator to

FIGURE 4 Architecture of the SE-Xception.



© Jifeng Wang, Penghu Li, Jie Yan, Liang Zhang, Hongwei Yi, Yuwei Deng, Haibo Huang

FIGURE 5 Architecture of the GAN.



© Jifeng Wang, Penghu Li, Jie Yan, Liang Zhang, Hongwei Yi, Yuwei Deng, Haibo Huang

minimize the statistical divergence separating the synthetic outputs from the ground-truth data. The two networks iterate continuously within this adversarial framework, ultimately converging to a Nash equilibrium, which endows the generated data with high authenticity and fidelity [50, 51].

However, GANs frequently encounter challenges during the training process, such as unstable convergence, loss function failure, a lack of sample diversity, and mode collapse [52, 53]. When the discriminator achieves an optimal state, the generator's optimization objective is to minimize the Jensen–Shannon (JS) divergence between the real data distribution P_d and the generated data distribution P_g as expressed in Equations 5 and 6. Here, P_1 and P_2 represent two probability distributions, and the JS divergence is employed to quantify their similarity [54]. Nevertheless, if the supports of P_d and P_g are disjoint, the JS divergence degenerates into a constant. This induces the vanishing gradient problem, which consequently compromises the stability of model training.

$$\mathrm{KL}\left(P_1 \,\|\, P_2\right) = \mathbb{E}_{x\sim P_1} \log \frac{P_1}{P_2} \tag{5}$$

$$\mathrm{JS}\left(P_1 \,\|\, P_2\right) = \frac{1}{2}\mathrm{KL}\left(P_1 \,\|\, \frac{P_1+P_2}{2}\right) + \frac{1}{2}\mathrm{KL}\left(P_2 \,\|\, \frac{P_1+P_2}{2}\right) \tag{6}$$

To address the aforementioned limitations, this article employs the WGAN architecture, substituting the traditional JS divergence with the Wasserstein distance. This modification fundamentally mitigates the instability encountered during the training process. The formulation is expressed as follows:

$$W\left(P_d, P_g\right) = \inf_{\gamma\sim\pi\left(P_d,P_g\right)} \mathbb{E}_{(x,y)\sim\gamma}\left[d\left(x-y\right)\right] \tag{7}$$

where $\pi(P_d,P_g)$ denotes the set of all joint probability distributions $\gamma(x,y)$ whose marginals correspond to the real distribution P_d and the generated distribution P_g, respectively. For any joint distribution γ within this set, it defines a transport plan from a real sample x to a generated sample y. The Wasserstein distance is mathematically formulated as the greatest lower bound of the expected distance $d(x,y)$ across all possible transport plans. Unlike the JS divergence, the Wasserstein distance remains capable of providing a continuous and smooth gradient metric even when the supports of the two distributions are disjoint [55]. With the introduction of this distance metric, the optimization objective function of the WGAN is formulated as Equation 8:

$$\min_{\theta_G}\max_{\theta_D} \mathbb{E}_{x\sim P_{\mathrm{data}}}\left[D\left(x\right)\right] + \mathbb{E}_{z\sim P_z}\left[\left(D\left(G\left(z\right)\right)\right)\right] \tag{8}$$

Compared to conventional GAN, the loss function of the WGAN more accurately quantifies the discrepancy between generated and authentic samples while effectively circumventing the vanishing gradient problem [56]. Consequently, the generator can more efficiently model the target data distribution, yielding a significant enhancement in the quality of the generated samples.

3. Experiment and Dataset Construction

3.1. Interior Wind Noise Testing

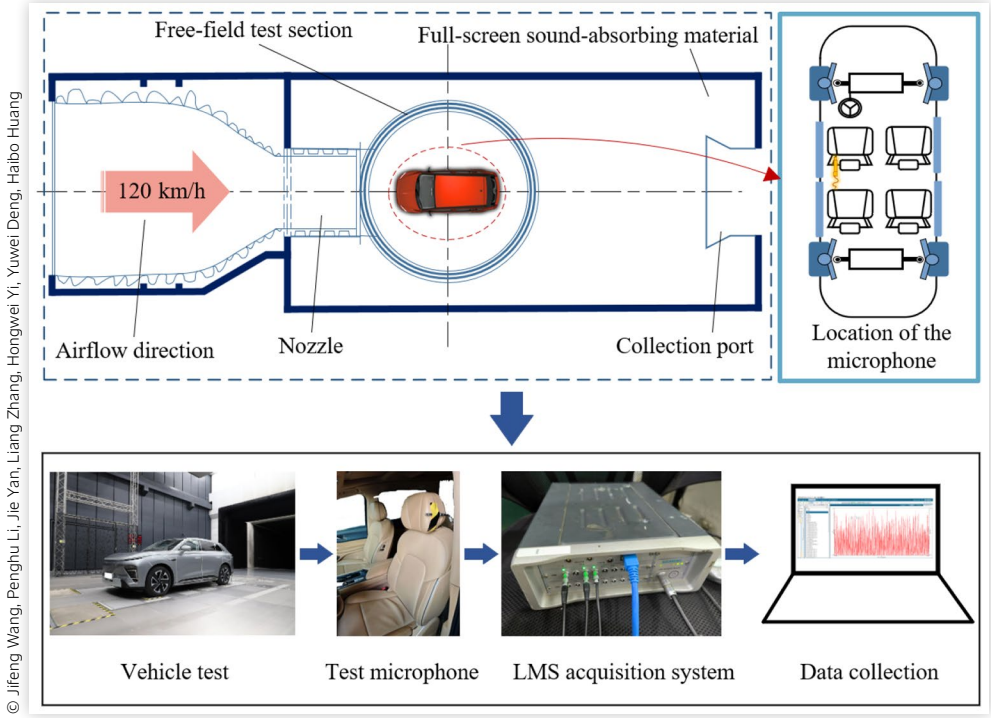
Automotive wind tunnels are dedicated to simulating vehicle operation in natural wind conditions and are extensively utilized during the engineering and optimization of automobile fluid dynamics and aeroacoustic characteristics [57]. Based on functional applications, they can be categorized into aeroacoustic wind tunnels and environmental wind tunnels [58]. Within this classification, aeroacoustic facilities are explicitly constructed to assess and evaluate both interior and exterior vehicle wind noise, serving as the principal experimental platform for wind noise development.

The interior noise measurements were conducted in the aforementioned aeroacoustic wind tunnel, and the detailed experimental setup is illustrated in Figure 6. To ensure flow symmetry around the vehicle, the test vehicle was positioned at the center of the wind tunnel test section, with the angle between the vehicle longitudinal symmetry plane and the wind tunnel centerline controlled within ±0.1°. The vehicle was secured using the parking brake, while all doors and windows remained closed. The air-conditioning system was switched to recirculation mode, and all air vents were closed to minimize interference from non-aerodynamic noise sources.

During the test, the wind speed was set to 120 km/h with a yaw angle of 0°. This operating condition was selected because aerodynamic noise becomes a dominant contributor to interior noise under high-speed cruising conditions. At elevated vehicle speeds, intensified flow separation, turbulent structures, and unsteady pressure fluctuations around the vehicle body significantly enhance aerodynamic excitation, making the influence of vehicle geometry and acoustic transmission characteristics on interior wind noise more pronounced. Moreover, 120 km/h represents a typical highway cruising condition and is widely adopted in vehicle NVH evaluations for wind noise assessment. Therefore, this condition provides an appropriate basis for investigating the relationship between vehicle design parameters and interior wind noise responses.

For acoustic data acquisition, a microphone was positioned on the left side of the driver's headrest to represent the driver's ear position. To cover the human auditory sensitive frequency range of 200–8000 Hz, the sampling frequency was set to 48 kHz, and each measurement

FIGURE 6 Driver's left ear noise test.



© Jifeng Wang, Penghu Li, Jie Yan, Liang Zhang, Hongwei Yi, Yuwei Deng, Haibo Huang

lasted for at least 15 s. During post-processing, the recorded sound pressure signals were corrected using A-weighting.

3.2. Vehicle Noise Test Results

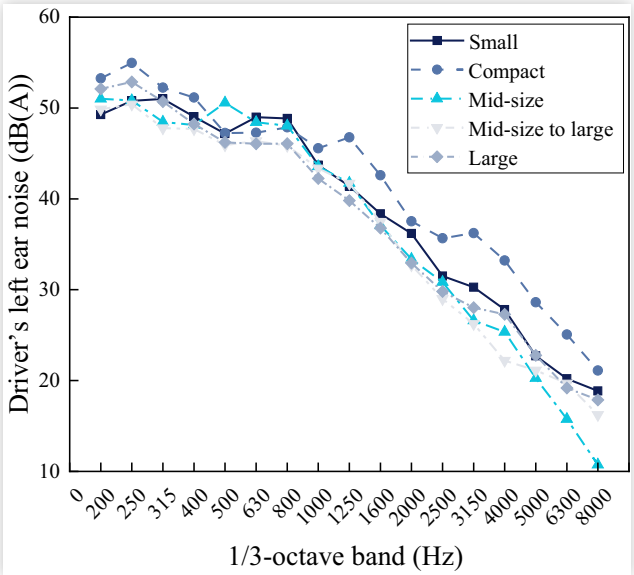
To guarantee that the acquired data encompasses a diverse range of SUV dimensions, a total of 50 test vehicles of varying sizes were selected for this experiment. Specifically, this cohort of 50 vehicles comprises 8 small SUVs under 4450 mm in length, 10 compact SUVs between 4450 mm and 4750 mm, 10 mid-size SUVs between 4750 mm and 4900 mm, 12 mid-to-large SUVs between 4900 mm and 5100 mm, and 10 large SUVs exceeding 5100 mm. The one-third-octave band sound pressure-level curves measured at the driver's left ear for each evaluated model are illustrated in Figure 7.

3.3. Analysis of Geometric Parameters Influencing Wind Noise

Directly utilizing the full-vehicle point cloud as the model input results in excessively high input dimensionality, which consequently exacerbates the demand for training samples. To reduce the input dimensionality, this article characterizes the overall vehicle styling through key styling parameters.

To ensure the aeroacoustic relevance of the selected styling parameters, steady-state CFD simulations were employed to analyze the influence of vehicle geometry on external flow characteristics and identify sensitive regions related to wind noise generation. Geometric variations can affect boundary layer development, flow separation, vortex structures, and wake evolution, leading to pressure fluctuations and aerodynamic excitation. Therefore, CFD-based flow analysis provides physical support for selecting key styling parameters.

FIGURE 7 Interior noise test results for different vehicle models.



© Jifeng Wang, Penghu Li, Jie Yan, Liang Zhang, Hongwei Yi, Yuwei Deng, Haibo Huang

TABLE 1 Physical model setup for steady-state simulation.

Parameter	Configuration
Fluid	Ideal gas
Turbulence model	Realizable k-ε model
Governing equations	Reynolds-averaged Navier–Stokes equation
Time formulation	Steady-state

© Jifeng Wang, Penghu Li, Jie Yan, Liang Zhang, Hongwei Yi, Yuwei Deng, Haibo Huang

Specifically, steady-state simulation results of the vehicle's external flow field were acquired using STAR-CCM+ software. Based on these results, the styling parameters that influence the generation of turbulence and vortices are systematically screened. The specific physical model configurations are detailed in Table 1.

Figure 8(a) illustrates the velocity streamline distribution of the external flow field around the test vehicle. Upon impinging on the front of the vehicle, the airflow separates into three primary streams: the first stream flows along the lateral sides of the front fascia, experiences flow separation and generates turbulence in the vicinity of the wheels, subsequently merges with the airflow near the fenders, and ultimately enters the wake region. The second stream is directed toward the underbody, where, due to the relatively flat chassis design, the airflow traverses this area smoothly, thereby mitigating the formation of complex underbody vortices. The remaining airflow is routed upward along the engine hood. Influenced by the height differential at the junction of the hood and the windshield, as well as the windshield wiper assembly, pronounced vortices are generated in this localized region. Subsequently, these vortices predominantly propagate along the A-pillar toward the rearview mirror region. A portion of the airflow bifurcates at the rearview mirror stalk, flowing, respectively, along the mirror triangle and the door surface toward the rear of the vehicle.

Figure 8(b) indicates the presence of a pronounced wake vortex behind the rearview mirror, situated in close proximity to the side window. During the processes of vortex breakdown and shedding, acoustic energy is released, concurrently inducing intense pressure fluctuations near the side window. This causes the glass to vibrate and generate aerodynamic noise, thereby allowing the wake vortex from the rearview mirror to exert a significant impact on side window wind noise. Figure 8(c) reveals a low-speed stagnation zone in front of the vehicle. The airflow accelerates markedly as it traverses the engine hood and roof, subsequently undergoing separation at the vehicle's rear to form a complex wake. The entrainment and shedding of these wake vortices release substantial acoustic energy and induce pressure fluctuations on the surfaces of the tailgate and rear window, thereby triggering structure-borne radiated noise. Figure 8(d) demonstrates that geometric abrupt changes in the A-pillar region lead to airflow acceleration and separation, forming a recirculation zone and shedding vortices behind the A-pillar. The continuous convection and breakdown of these vortices not only amplify the local aeroacoustic energy but also excite fluctuating pressures on the side window surface, inducing forced vibration of the glass. The A-pillar region, therefore, constitutes a critical source of interior aerodynamic noise.

In summary, this article partitions the vehicle body into the A-pillar region, longitudinal symmetry plane, and the rearview mirror region. Based on engineering experience, the key styling parameters selected for analysis are detailed in Table A.1.

Furthermore, considering the significant influence of vehicle acoustic structures, including glazing materials, sealing systems, and interior acoustic components, on the transmission of aerodynamic noise [59, 60], acoustic transfer functions (ATFs) were introduced as input features to characterize the transfer characteristics from external aerodynamic excitation to interior noise responses at the driver's position.

The ATFs used in this study were obtained through vehicle acoustic measurements. Since interior wind noise is affected not only by external aerodynamic excitation but also by structural transmission paths, glazing insulation performance, and the interior acoustic environment, experimentally measured ATFs can comprehensively represent the attenuation characteristics of the vehicle acoustic package system. The ATF is defined as the frequency response relationship between the interior sound pressure response at the target measurement point and the external excitation sound pressure:

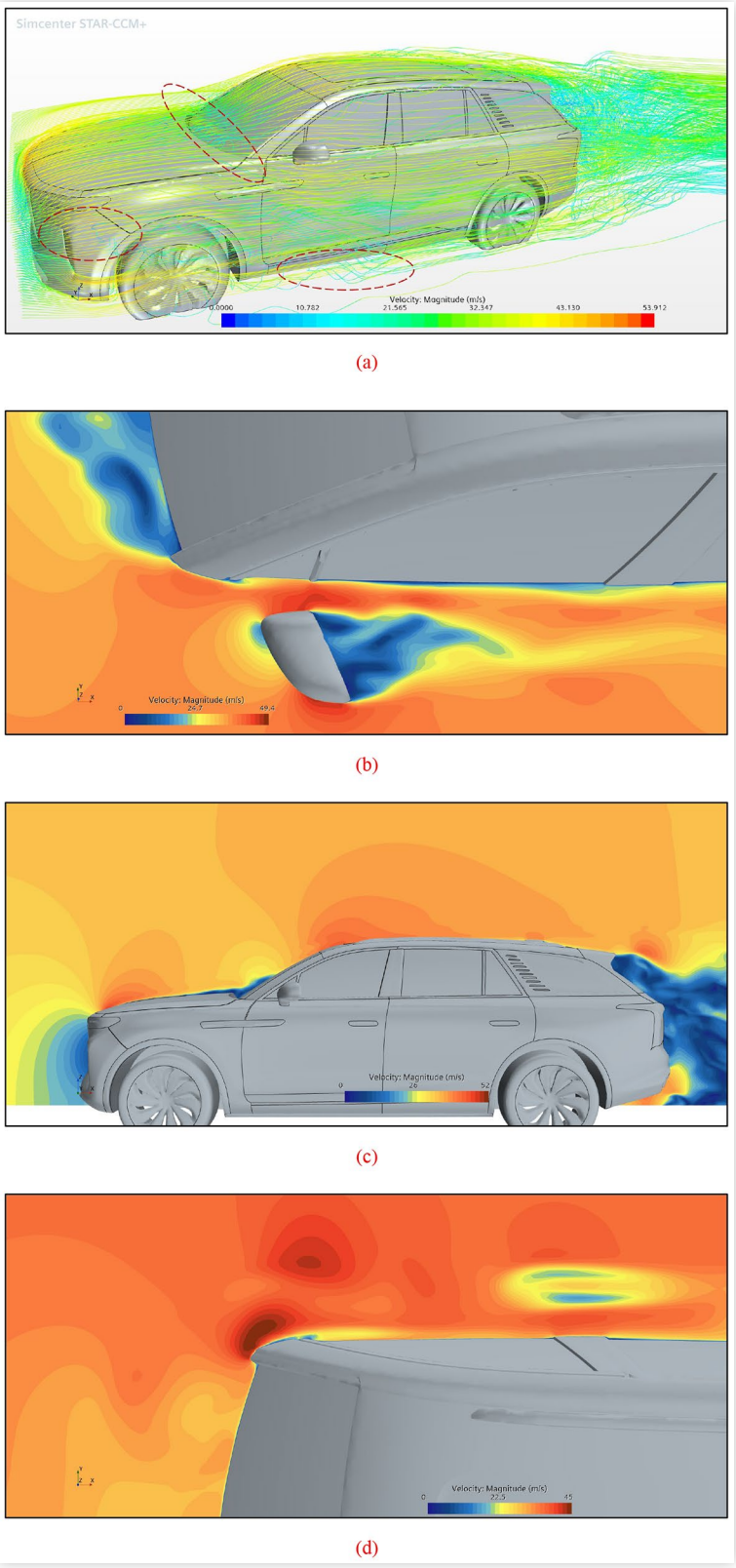
$$H(f) = \frac{P_{\text{in}}(f)}{P_{\text{out}}(f)} \tag{9}$$

where $P_{\text{in}}(f)$ represents the interior sound pressure spectrum measured at the driver's left ear position, $P_{\text{out}}(f)$ denotes the input sound pressure spectrum measured at the external reference position of the vehicle, and $H(f)$ represents the frequency-dependent transfer characteristics of the vehicle acoustic transmission path.

During testing, broadband acoustic excitation was applied to the vehicle, while sound pressure responses at the external reference position and driver's ear position were simultaneously recorded. The ATFs in 17 one-third-octave bands were extracted through frequency-domain analysis and used as input variables, rather than a single averaged value, to preserve frequency-dependent acoustic transmission characteristics.

Consequently, the constructed dataset consists of 29 vehicle styling parameters and 17 one-third-octave ATF features as inputs, with 17 one-third-octave interior wind noise levels measured at the driver's left ear position as outputs. This configuration enables the model to capture the nonlinear relationship among vehicle design parameters, acoustic transmission characteristics, and interior wind noise responses.

FIGURE 8 Steady-state simulation results. (a) Velocity streamlines of the external flow field around the full vehicle. (b) Velocity streamlines at the cross-section of the side mirror. (c) Velocity contours on the vehicle's longitudinal symmetry plane. (d) Velocity contours in the A-pillar region of the vehicle.



© Jifeng Wang, Penghu Li, Jie Yan, Liang Zhang, Hongwei Yi, Yuwei Deng, Haibo Huang

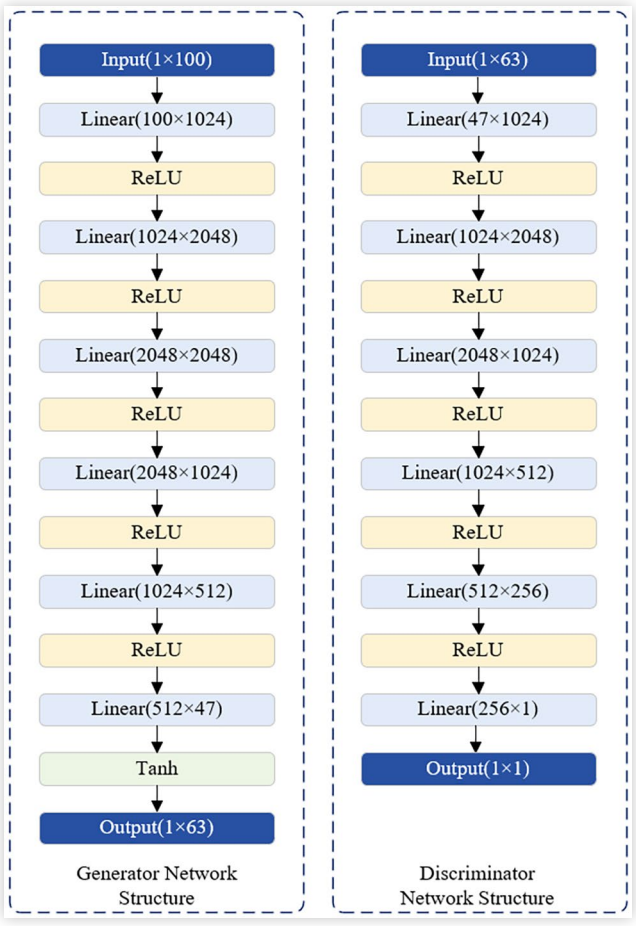
4. Data Enhancement Based on GAN

4.1. Construction of the WGAN

The architecture of the generator and discriminator employed in the WGAN is illustrated in Figure 9. To ensure the diversity of generated samples while mitigating issues such as computational redundancy and difficulties in feature convergence arising from high-dimensional spaces, the input to the generator is a 1×100 random noise vector sampled from a Gaussian distribution. This vector serves as the initial latent feature and subsequently passes through five hidden layers, each incorporating Batch Normalization and ReLU activation, to facilitate the deep mapping of the generated data. Ultimately, the network utilizes a Tanh activation function to output a 1×63 composite feature vector, where the first 46 dimensions correspond to the 29 styling parameters and 17 one-third-octave ATF features, while the remaining 17 dimensions correspond to the wind noise levels across the 17 frequency bands.

During the training process of the WGAN, the model was configured for a total of 2000 epochs, utilizing the Adam optimizer to alternately optimize the generator and the discriminator. In each network iteration, the discriminator undergoes five independent training sessions, followed by one iteration of updates for the generator. After 2000 adversarial iterations, the generator exhibited excellent distribution fitting performance, enabling the efficient and high-fidelity augmentation of the small-sample dataset comprising SUV styling parameters and their corresponding wind noise characteristics.

FIGURE 9 Architecture of the WGAN generator and discriminator.



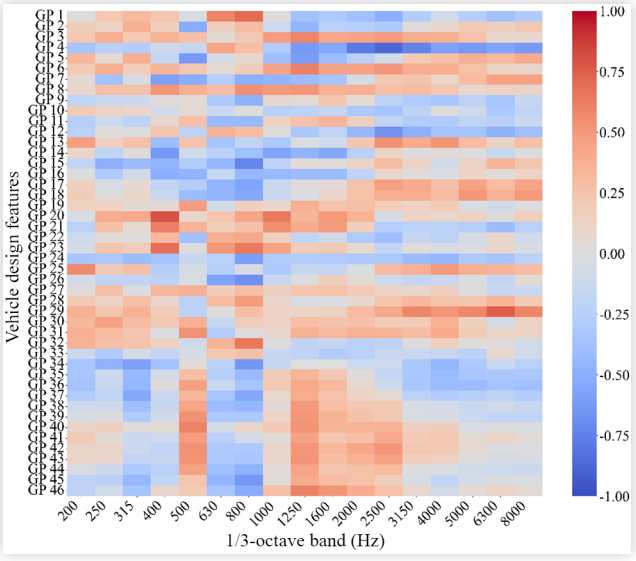
© Jifeng Wang, Penghu Li, Jie Yan, Liang Zhang, Hongwei Yi, Yuwei Deng, Haibo Huang

4.2. Analysis of Data Augmentation Results

Given that the relationship between styling parameters and wind noise is highly nonlinear, we utilized the Pearson coefficient to evaluate the generation quality of the developed WGAN. This analysis was performed on both the original small-sample dataset and the augmented dataset expanded via the WGAN. Figures 10 and 11 depict the heatmaps illustrating the correlation matrices between the geometric parameters and the frequency bands. In these visualizations, GP1 denotes the first geometric parameter, corresponding to the X-direction dimension of the upper A-pillar. Table A.1 provides a comprehensive list of all specific geometric parameters, including their detailed nomenclature and corresponding codes.

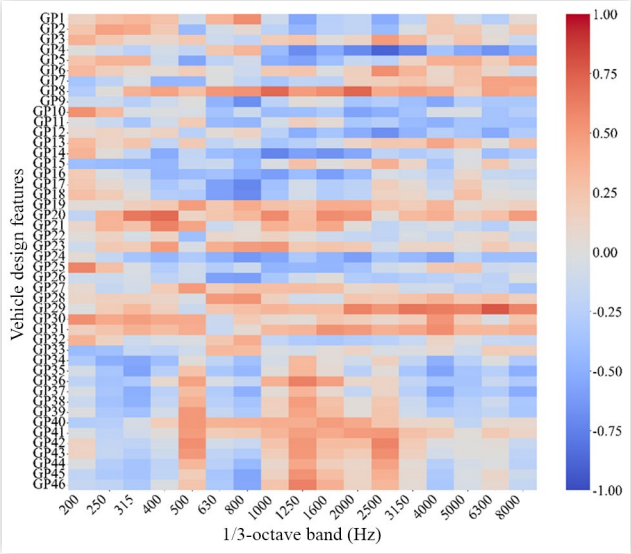
To further evaluate whether the WGAN-generated samples preserve the statistical characteristics of the original dataset, Pearson correlation matrices between vehicle styling parameters and wind noise responses were

FIGURE 10 Correlation heatmap of the original data.



© Jifeng Wang, Penghu Li, Jie Yan, Liang Zhang, Hongwei Yi, Yuwei Deng, Haibo Huang

FIGURE 11 Correlation heatmap of the generated data.



© Jifeng Wang, Penghu Li, Jie Yan, Liang Zhang, Hongwei Yi, Yuwei Deng, Haibo Huang

calculated for both datasets, as illustrated in Figures 10 and 11. It should be noted that Pearson correlation analysis mainly characterizes linear dependencies between variables and cannot independently verify the complete distribution consistency of high-dimensional data. Therefore, it was employed as a statistical indicator to evaluate whether the generated samples retain the major correlation patterns embedded in the original dataset.

As shown in Figures 10 and 11, the generated dataset exhibits a similar overall correlation distribution compared with the original dataset. The dominant positive and negative correlation trends between styling parameters and wind noise responses across different frequency bands are consistently maintained. For example, several key geometric parameters show comparable correlation characteristics in the low-frequency range of 315–500 Hz, while similar correlation tendencies are also preserved in the middle-to-high-frequency range. These results indicate that the WGAN successfully captures the major statistical relationships between vehicle styling features and acoustic responses rather than simply reproducing existing samples.

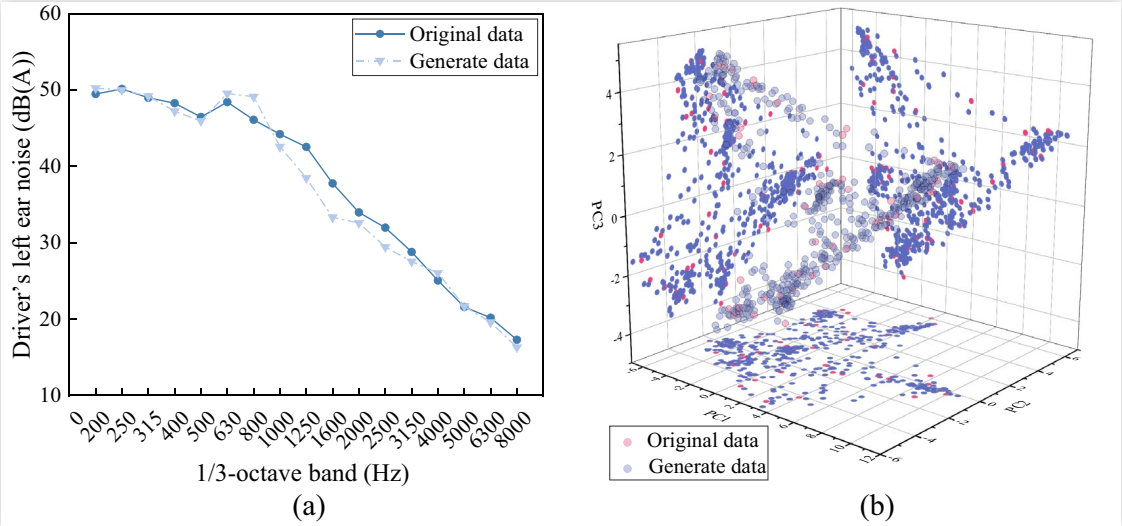
However, Pearson correlation only reflects linear relationships and cannot fully describe nonlinear dependencies or the global distribution characteristics of high-dimensional data. Therefore, PCA-based distribution analysis was further conducted to evaluate the consistency between generated and original datasets in latent feature space.

To further assess the distributional consistency of the generated data, the distributions of input and output data were evaluated separately. Figure 12(a) presents a comparison between randomly sampled original noise curves and generated ones, where the noise curves exhibit consistent trends while maintaining distinct paths, indicating that the generated data possesses both diversity and flexibility.

In addition to the curve-level comparisons, principal component analysis (PCA) was performed [61] to evaluate whether the generated samples capture the global distribution characteristics of the original dataset. Unlike Pearson correlation analysis, which focuses on pairwise linear relationships, PCA provides a representation of the overall structural characteristics of high-dimensional data by extracting dominant variation directions.

As shown in Figure 12(b), the original and generated samples exhibit highly similar distribution patterns in the

FIGURE 12 Comparison between original and generated data. (a) Comparison between original and generated noise. (b) Comparison between original and generated styling data.



© Jifeng Wang, Penghu Li, Jie Yan, Liang Zhang, Hongwei Yi, Yuwei Deng, Haibo Huang

reduced-dimensional PCA space. The generated samples are located within the distribution range of the original dataset rather than forming an isolated cluster, indicating that the WGAN successfully captures the major variation characteristics of the original data domain.

These results indicate that the WGAN-generated samples maintain the essential statistical characteristics and distribution patterns of the original dataset. The combination of correlation analysis and PCA-based distribution evaluation provides complementary evidence that the generated samples preserve both variable-level relationships and global feature structures. Therefore, the WGAN-based augmentation strategy can effectively expand the available training data under small-sample conditions while maintaining consistency with the original data domain.

5. Interior Wind Noise Prediction at the Driver's Position Based on SE-Xception

5.1. Construction of the SE-Xception

The SE-Xception model proposed in this article incorporates the attention mechanism into depthwise separable convolutions. The complete network architecture is illustrated in Figure 4, and detailed network configuration parameters, along with the output dimensions for each layer, are presented in Table 2.

TABLE 2 Network parameter settings.

Layer	Parameter name	Parameter size	Output size
Input	—	—	[1, 30]
Input Conv	Kernel, padding, stride	3, 1, 1	[64, 30]
SE-Xception Block 1	Channel, stride, reduction ratio	(64, 128), 1, 8	[128, 30]
SE-Xception Block 2	Channel, stride, reduction ratio	(128, 256), 2, 8	[256, 15]
SE-Xception Block 3	Channel, stride, reduction ratio	(256, 512), 1, 8	[512, 15]
SE-Xception Block 4	Channel, stride, reduction ratio	(512, 512), 2, 8	[512, 8]
Global AvgPooling	Output length	1	[512, 1]
Flatten	—	—	[512]
Linear 1	Channel	(512, 256)	[256]
Linear 2	Channel	(256, 128)	[128]
Linear 3	Channel	(128, 17)	[17]

© Jifeng Wang, Penghu Li, Jie Yan, Liang Zhang, Hongwei Yi, Yuwei Deng, Haibo Huang

The dataset utilized in this study comprises 300 samples generated via the WGAN framework detailed in Section 4.

In order to substantiate the algorithmic superiority of the SE-Xception architecture, an explicit performance evaluation was conducted against three representative neural network architectures: Xception, temporal convolutional network (TCN), and transformer. For each, a dedicated interior noise prediction model was developed. The Xception model maintains the same global architecture as SE-Xception, with the distinction that the SE modules are omitted from its depthwise separable convolution blocks. The TCN architecture comprises five temporal convolutional layers (with output channels of 64, 128, 256, 512, and 512, utilizing 3×3 causal kernels and dilation factors of 1, 2, 4, 8, and 16, respectively), which subsequently transition into an adaptive average downsampling block and a terminal dense layer. The transformer architecture features a front end consisting of two 1D convolutional layers (input channels of 1 and 64, respectively, with 3×3 kernels and padding = 1), followed by four transformer encoder layers (128 hidden dimensions, 8 attention heads). During training, all models were subjected to five-fold cross-validation using an identical dataset.

Furthermore, to verify the effectiveness of introducing the SE module in improving interior wind noise prediction performance and to determine whether the performance enhancement originates from the channel attention mechanism rather than merely an increase in network parameters, an ablation study was conducted. Two models were constructed for comparison: the proposed SE-Xception model and a parameter-matched Xception model. The latter removed the SE module and increased the parameters of the fully connected layers to maintain a comparable number of trainable parameters with the SE-Xception model, thereby ensuring similar model complexity between the two architectures.

To ensure the reliability of the model evaluation, a five-fold cross-validation approach was employed. Within each fold, 240 samples were allocated for training, while 60 were reserved for validation. Model hyperparameters and training strategies were finalized based on the average performance across these five folds. For an objective performance contrast across different architectures and to objectively gauge their reliability, the mean absolute percentage error (MAPE) and the root mean square error (RMSE) were adopted as the fundamental quantitative benchmarks for appraising inferential accuracy. All network construction and numerical simulations were conducted on a workstation equipped with an AMD Ryzen 7 7700 CPU and 64 GB of RAM.

5.2. Model Performance Comparison

Table 3 summarizes the comparative evaluation of predictive fidelity across the five distinct network architectures utilizing this dataset.

TABLE 3 Error comparison of various models on the same dataset.

Model	Mean five-fold MAPE (%)	Mean five-fold RMSE (dB)
Xception	1.98	0.71
Transformer	1.88	0.70
TCN	1.83	0.69
SE-Xception	1.47	0.56
Parameter-matched Xception	1.94	0.70

© Jifeng Wang, Penghu Li, Jie Yan, Liang Zhang, Hongwei Yi, Yuwei Deng, Haibo Huang

A comparison of the performance of the various models across the same dataset reveals that all models exhibit relatively low error, indicating that each of the five architectures maintains robust stability and generalization capabilities regardless of the specific data partitioning.

Figure 13 illustrates the absolute error distributions of different models on the validation set, where the error bars denote the standard deviations of prediction errors and reflect the variation of model outputs. Although all models exhibit certain wind noise prediction capability across different frequency bands, differences can be observed in terms of accuracy and stability.

The Xception and Parameter-matched Xception models show relatively limited generalization performance. Both models achieve low errors in the low-frequency range below 500 Hz; however, the prediction errors gradually increase with increasing frequency. In particular, the errors become more significant above 5000 Hz, with maximum errors exceeding 1.1 dB, indicating that conventional convolutional architectures may have limitations in capturing complex high-frequency aeroacoustic characteristics.

The Transformer and TCN models reduce prediction errors in some frequency bands due to their ability to model long-range dependencies and temporal patterns. Nevertheless, noticeable local fluctuations remain in their error distributions. The Transformer model improves high-frequency prediction performance but exhibits a maximum error of approximately 1.4 dB at 1250 Hz. The TCN model performs relatively well in the 500–1000 Hz range but presents larger errors at 1600–2000 Hz and 4000 Hz, with the error exceeding 1.3 dB at 4000 Hz.

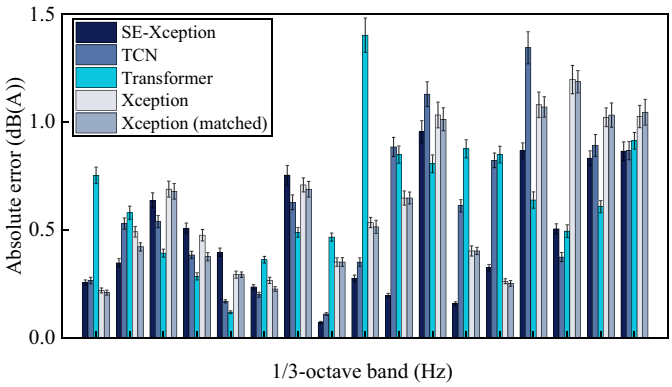
In comparison, the proposed SE-Xception model achieves improved overall prediction accuracy and stability. The comparison with Xception and Parameter-matched Xception demonstrates that the SE module contributes to performance improvement by adaptively weighting frequency-related features rather than simply increasing network parameters. The SE-Xception model presents a more balanced error distribution, with smaller error variations across most frequency bands. Except for the region near 2000 Hz, where the error approaches 1.0 dB, the absolute errors remain below 0.8 dB at most frequencies. These results validate the efficacy of the proposed method for aerodynamic noise prediction.

5.3. Generalization Performance Evaluation of the SE-Xception Model

To further evaluate the generalization capability of the proposed framework under practical engineering conditions, three completely unseen SUV models were selected for external validation. These vehicles were not involved in the construction of the original dataset, the WGAN-based data augmentation process, or model training, and were used exclusively to assess the prediction capability under unknown vehicle design conditions. The selected validation vehicles include compact, midsize, and mid-to-large SUVs, covering different vehicle sizes and styling characteristics to a certain extent.

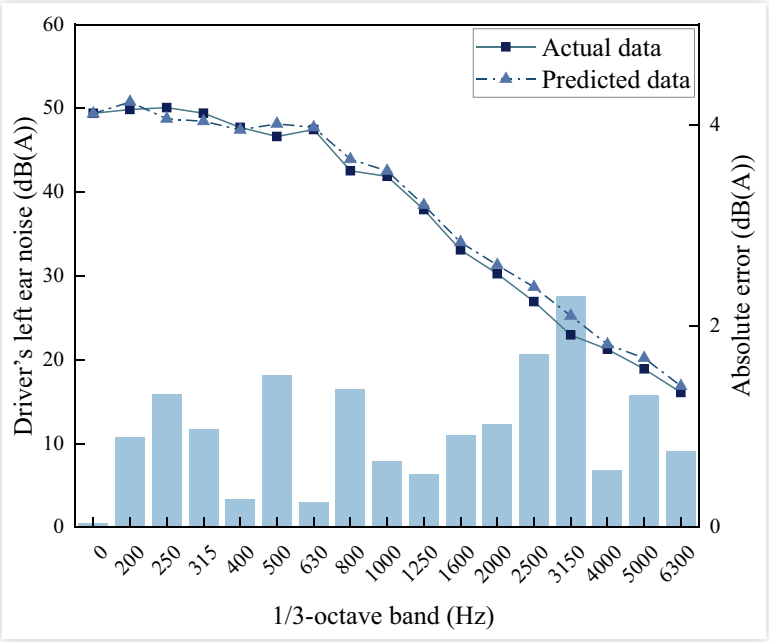
Figures 14, 15, and 16 present comparisons between the predicted and measured interior wind noise spectra

FIGURE 13 Prediction performance of different network architectures. Xception (Matched) denotes the parameter-matched Xception.



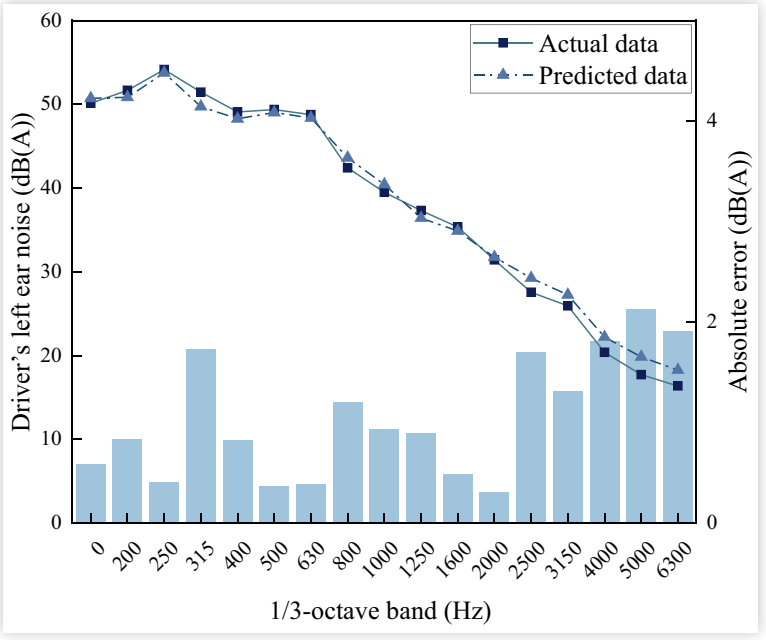
© Jifeng Wang, Penghu Li, Jie Yan, Liang Zhang, Hongwei Yi, Yuwei Deng, Haibo Huang

FIGURE 14 Prediction results of the SE-Xception for the compact SUV.



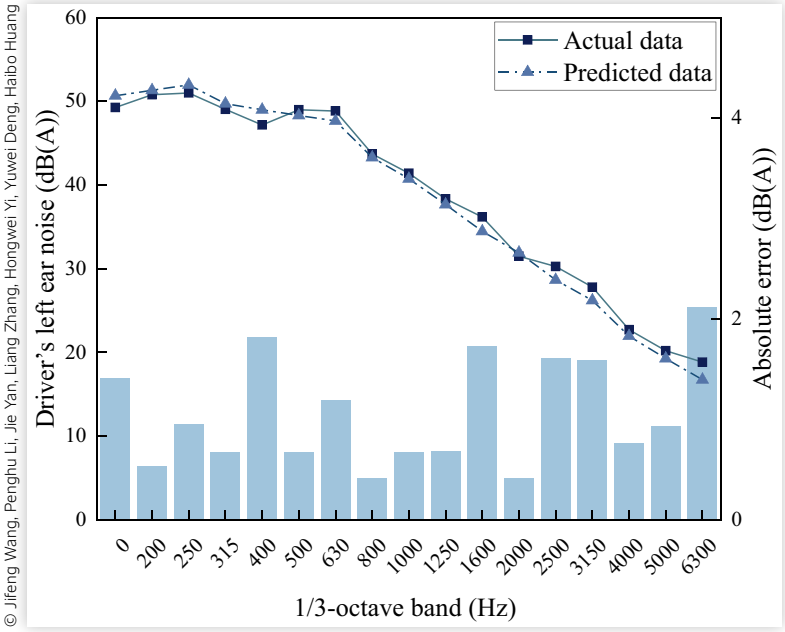
© Jifeng Wang, Penghu Li, Jie Yan, Liang Zhang, Hongwei Yi, Yuwei Deng, Haibo Huang

FIGURE 15 Prediction results of the SE-Xception for the mid-size SUV.



© Jifeng Wang, Penghu Li, Jie Yan, Liang Zhang, Hongwei Yi, Yuwei Deng, Haibo Huang

FIGURE 16 Prediction results of the SE-Xception for the mid-to-large SUV.



of the three independent validation vehicles using the SE-Xception model. The results demonstrate that the proposed model can effectively capture the overall spectral variation trends of interior wind noise for different vehicle types while maintaining stable prediction performance across all validation cases. The average MAPE values for the three validation vehicles are 3.18%, 3.75%, and 3.26%, respectively, while the corresponding average RMSE values are 1.12 dB, 1.20 dB, and 1.19 dB.

Combined with the previous analysis of the distribution consistency and diversity of generated samples, the WGAN-augmented dataset increases the coverage of training data and contributes to improving the model's adaptability to unseen vehicle conditions. Meanwhile, the SE-Xception model is capable of extracting nonlinear relationships between vehicle styling parameters and interior wind noise responses. Therefore, the proposed framework demonstrates promising prediction stability and generalization capability when applied to vehicle designs that are not included in the model development process.

5.4. Sensitivity Analysis

To improve the physical interpretability of the prediction results, the mean impact value (MIV) method was further employed to quantitatively evaluate the importance of input geometric parameters. Although the vehicle acoustic transfer functions (ATFs) were introduced as input features to characterize the attenuation characteristics during the propagation of external aerodynamic noise to the driver's ear position, they mainly represent differences in acoustic transmission paths rather than the influence of exterior geometry on aerodynamic noise generation. Therefore, in the sensitivity analysis of styling parameter contributions, the ATFs were fixed as boundary conditions to avoid interference from acoustic configuration variations on the evaluation of geometric parameter importance.

Specifically, while maintaining constant ATF inputs, positive and negative perturbations were applied individually to each styling parameter. The corresponding changes in predicted wind noise responses were then calculated using the trained SE-Xception model. By comparing the variations in predicted sound pressure levels caused by different geometric parameter perturbations, the influence of each parameter on wind noise responses in different one-third-octave frequency bands was quantified.

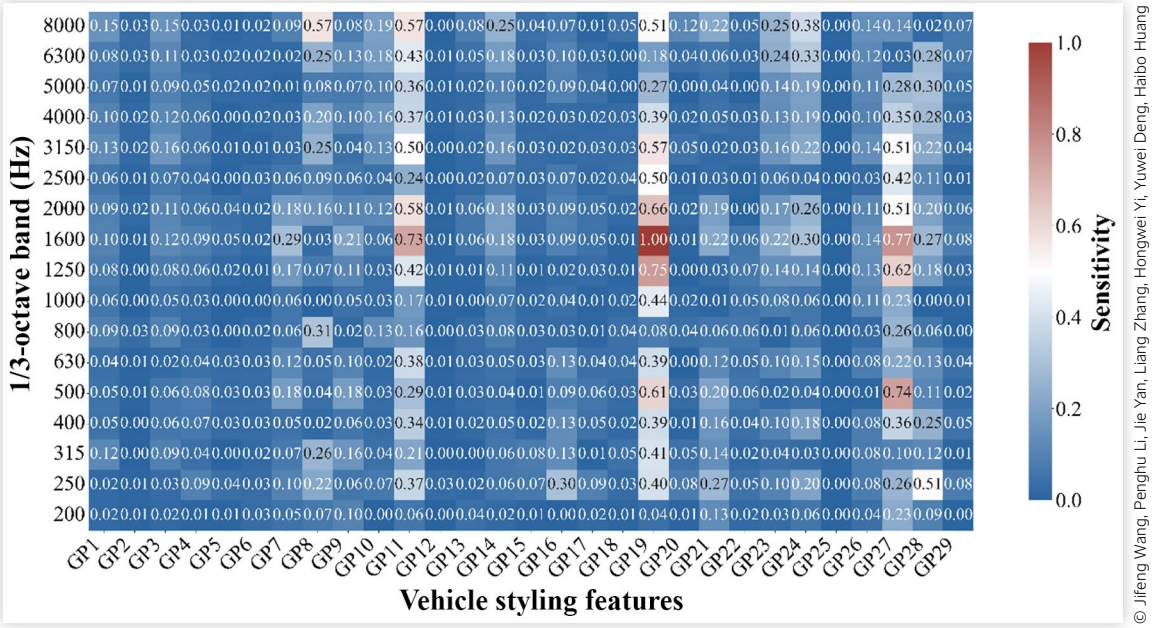
The MIV method is an effective approach for evaluating feature importance in neural networks. After model training, this method introduces controlled perturbations to the original input features and assesses their contributions by measuring the resulting changes in model outputs. The calculation process is expressed as follows:

$$\mathrm{MIV} = \frac{1}{N_S}\sum_{i=1}^{N_S} y_i\left(X_{X_V+10\%}\right) - y_i\left(X_{X_V-10\%}\right) \tag{10}$$

where N_s represents the frequency range of the independent variable, X_v indicates the base value of the independent variable, $y_i(X_{X_v + 10\%})$ denotes the predicted result when the variable is increased by 10%, and $y_i(X_{X_v - 10\%})$ denotes the predicted result when decreased by 10%.

Figure 17 presents the MIV distributions of the 29 vehicle styling parameters across different one-third-octave frequency bands. The results indicate that the effects of different styling parameters on interior wind

FIGURE 17 Full-frequency sensitivity analysis.



© Jifeng Wang, Penghu Li, Jie Yan, Liang Zhang, Hongwei Yi, Yuwei Deng, Haibo Huang

noise responses exhibit clear frequency-dependent characteristics. Among them, the trailing-edge angle of the exterior mirror (Geometric parameter 11) shows relatively high sensitivity in the 1000–2500 Hz frequency range, suggesting its important influence on mid-to-high frequency wind noise. This can be attributed to the fact that variations in the mirror trailing-edge angle may alter local flow separation characteristics and wake vortex structures, thereby affecting unsteady pressure fluctuations.

In addition, the spatial angle parameters of the A-pillar (Geometric parameters 26–28) exhibit relatively high MIV values in the 1000–4000 Hz range, indicating that the three-dimensional geometric configuration of the A-pillar has a considerable influence on aerodynamic noise generation near the side window region. In contrast, local A-pillar dimensional parameters and windshield curvature show relatively lower sensitivity, suggesting that their effects on airflow characteristics are limited within the investigated parameter ranges. The windshield inclination angle (Geometric parameter 19) demonstrates higher sensitivity in the 1250–2000 Hz range, which may be related to its influence on pressure distribution and flow characteristics around the windshield–A-pillar junction.

Overall, the MIV analysis results show good consistency with vehicle aeroacoustic mechanisms, indicating that the proposed model not only provides wind noise prediction capability but also enables the identification of critical styling-sensitive parameters. This provides a theoretical reference for wind noise-oriented optimization during the early stage vehicle styling design process.

5.5. Impact of Generated Sample Size on Prediction Model Accuracy

Within the training mechanism of the WGAN, the generator and discriminator are optimized through an adversarial process, compelling the generator to progressively learn the underlying patterns of the real data distribution, thereby producing highly similar sample data [62]. Although the generated data approximates the real dataset in its statistical characteristics, distributional discrepancies persist between the synthetic and original samples. To systematically examine the influence of the generated sample size on the model's predictive performance, this study manipulated the generator model to construct augmented datasets comprising 50, 100, 200, 300, 400, and 500 samples, respectively. Utilizing these generated datasets, the SE-Xception predictive model was trained via five-fold cross-validation, and its predictive efficacy was subsequently evaluated using an independent experimental validation vehicle. The final results are presented in Table 4.

A comparison of the SE-Xception model's performance across datasets of varying scales reveals that its predictive accuracy is highly dependent on the number of generated samples. Evaluated on the validation vehicle, the model's predictive precision progressively enhances with the initial accumulation of WGAN-generated samples. When trained with 50 generated samples, the model yields a MAPE of 5.50% and an RMSE of 1.88 dB. As the sample size increases, both error metrics steadily improve, with the MAPE and RMSE decreasing to 4.28% and 1.52 dB, respectively, at 100 generated samples. These metrics

TABLE 4 Prediction error versus the size of generated samples.

Generated samples	Mean five-fold MAPE (%)	Mean five-fold RMSE (dB)	Test vehicle MAPE (%)	Test vehicle RMSE (dB)
50	2.32	0.82	5.50	1.88
100	1.18	0.45	4.28	1.52
200	0.92	0.41	3.68	1.29
300	0.77	0.36	3.26	1.19
400	0.72	0.29	4.29	1.57
500	0.68	0.25	4.65	1.82

© Jifeng Wang, Penghu Li, Jie Yan, Liang Zhang, Hongwei Yi, Yuwei Deng, Haibo Huang

reach their absolute minimum at 300 generated samples, achieving a MAPE of 3.26% and an RMSE of 1.19 dB, which marks the model's optimal performance. This trend demonstrates that augmenting the generated data volume within a specific threshold exerts a profoundly positive impact on predictive capabilities. However, once the number of generated samples exceeds 300, both the MAPE and RMSE exhibit an upward trajectory. For instance, at 400 generated samples, the MAPE and RMSE increase to 4.29% and 1.57 dB, respectively. A further expansion to 500 samples elevates the MAPE to 4.65% and the RMSE to 1.82 dB. This reversal suggests that an excessive volume of synthetic samples may induce model overfitting, prompting the network to memorize inherent dataset noise rather than extracting effective underlying features.

Figure 18 illustrates the influence of augmented sample size on the prediction error distribution of the proposed model. When only a limited number of augmented samples (50 and 100 samples) are introduced, relatively large absolute errors are observed over most frequency bands, particularly in the high-frequency region. This suggests that insufficient augmented data cannot provide adequate coverage of the vehicle acoustic response characteristics, thereby limiting the model's ability to learn the complex nonlinear relationship between vehicle parameters and interior wind noise.

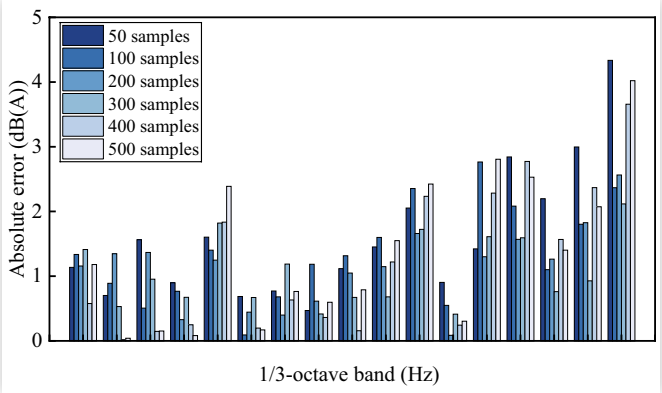
With the increase in augmented sample size from 200 to 300 samples, the prediction errors are consistently reduced across most frequency bands. Among all tested augmentation scales, the model trained with 300 augmented samples achieves the lowest overall error level, with the absolute errors at most frequency bands maintained below 2 dB. This indicates that an appropriate amount of generated data can effectively enrich the training distribution and improve the model's prediction robustness.

However, further increasing the augmented samples to 400 and 500 does not lead to additional performance improvement. Instead, increased errors can be observed in several frequency ranges, especially around 500 Hz and the high-frequency bands from 3150 Hz to 8000 Hz. This phenomenon may be attributed to the introduction of redundant or less representative generated samples, which weakens the effectiveness of data augmentation. Therefore, an excessive expansion of the augmented dataset does not necessarily improve model performance, and an appropriate augmentation scale is essential for achieving optimal prediction accuracy.

To further clarify the independent contributions of measured data and WGAN-generated data to the prediction performance, this study investigated the influence of different data sources by varying the amount of real measurement data and separating real and generated samples during model training.

First, to evaluate the impact of the amount of real measurement data on model performance, the original 50 experimental samples were reduced to 30 samples, and a new WGAN model was trained based on these 30 real samples to generate augmented data. Subsequently, with the prediction model architecture and training configurations kept consistent, different WGAN-augmented datasets were used for model training and compared with the dataset generated from 50 real samples. The results are presented in Table 5.

FIGURE 18 Prediction error of the model for test vehicles under varying generated sample sizes.



© Jifeng Wang, Penghu Li, Jie Yan, Liang Zhang, Hongwei Yi, Yuwei Deng, Haibo Huang

TABLE 5 Comparison of model performance using different original sample sizes

Generated samples	30 Original samples MAPE (%)	30 Original samples RMSE (dB)	50 Original samples MAPE (%)	50 Original samples RMSE (dB)
50	5.61	1.93	5.50	1.88
100	4.43	1.64	4.28	1.52
200	3.74	1.32	3.68	1.29
300	3.83	1.44	3.26	1.19
400	4.42	1.68	4.29	1.57
500	4.85	1.91	4.65	1.82

© Jifeng Wang, Penghu Li, Jie Yan, Liang Zhang, Hongwei Yi, Yuwei Deng, Haibo Huang

The results indicate that reducing the number of real measured samples from 50 to 30 leads to an increase in the overall prediction error of the model. This demonstrates that the scale of real measurement data plays an important role in determining model prediction performance. Since real vehicle data contain actual combinations of styling parameters and their corresponding acoustic responses, reducing the number of measured samples decreases the coverage of the original wind noise distribution in the training data, thereby limiting the model's generalization capability.

To further distinguish the contributions of real measured data and WGAN-generated data to model performance, the real samples in the augmented dataset were removed, and only WGAN-generated samples were retained for model training. Specifically, a WGAN model was trained using the 50 real samples to generate the corresponding augmented dataset. The original measured samples were then excluded, and the SE-Xception prediction model was trained solely using the generated samples. The results are presented in Table 6.

Overall, the prediction performance of the model is jointly influenced by the quantity of real measurement data and the quality of generated samples. A reduction in the number of real samples leads to decreased prediction accuracy, as the training data may provide insufficient coverage of the vehicle styling parameter space and the corresponding wind noise response distribution. Under the same amount of real measurement data, the introduction of WGAN-generated samples effectively reduces prediction errors, indicating that the generated samples provide additional distributional information rather than simply introducing random perturbations. However, an excessively high proportion of generated samples may also degrade model performance. This is because the inevitable minor discrepancies between the WGAN-generated distribution and the real data distribution can be amplified as the proportion of synthetic samples increases, causing the model to become more biased toward the generated data distribution and consequently reducing its generalization capability.

TABLE 6 Analysis of the contribution of real measurement data.

Generated samples	Including original data MAPE (%)	Including original data RMSE (dB)	Excluding original data MAPE (%)	Excluding original data RMSE (dB)
50	5.50	1.88	5.75	2.03
100	4.28	1.52	4.63	1.77
200	3.68	1.29	3.83	1.46
300	3.26	1.19	3.79	1.35
400	4.29	1.57	4.52	1.75
500	4.65	1.82	4.97	1.83

© Jifeng Wang, Penghu Li, Jie Yan, Liang Zhang, Hongwei Yi, Yuwei Deng, Haibo Huang

Based on the preceding analysis, it is concluded that generating 300 samples, which is equivalent to six times the size of the original dataset, yields the optimal predictive results for the wind noise prediction problem. This balance effectively enhances predictive fidelity while concurrently suppressing the potential for generalization degradation.

5.6. Comparison of Different Data Augmentation Strategies

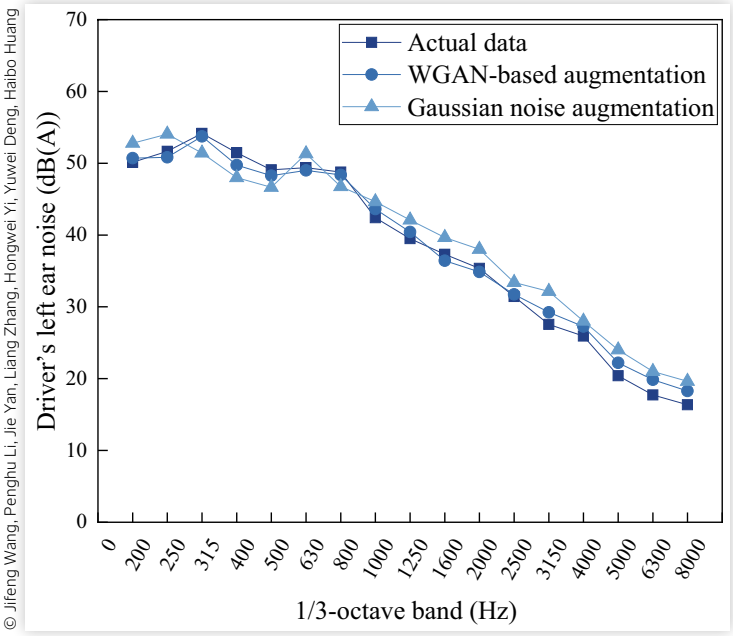
To further validate the effectiveness of the proposed WGAN-based data augmentation strategy, a comparative experiment was conducted using a conventional Gaussian noise injection method. Gaussian noise augmentation is a commonly used data expansion technique that generates additional samples by introducing random perturbations into the original data. In this comparison, the noise intensity was set to 1.5%.

To ensure a fair and rigorous comparison, Gaussian noise injection and WGAN were separately employed to generate augmented datasets with the same number of samples. Subsequently, the SE-Xception model was trained using the two augmented datasets while maintaining identical model architecture, training strategy, and hyperparameter settings. The prediction performance of the models trained with different augmentation strategies was then evaluated using the same independent validation vehicle dataset to quantitatively compare their effects on prediction accuracy and generalization capability.

Figure 19 presents the prediction results obtained using the two augmentation strategies. The results show that both models can capture the overall spectral variation trends of interior wind noise, which are highly consistent with the measured data. This indicates that data augmentation contributes to improving the model's ability to characterize frequency-dependent wind noise patterns.

However, across most one-third-octave frequency bands, the WGAN-based augmentation strategy achieves higher consistency with the measured data. Particularly in the mid-to-high-frequency range, where aerodynamic noise generation mechanisms are more complex, the predictions obtained using WGAN-enhanced data exhibit

FIGURE 19 Comparison of results from different data augmentation strategies.



© Jifeng Wang, Penghu Li, Jie Yan, Liang Zhang, Hongwei Yi, Yuwei Deng, Haibo Huang

smaller deviations from the experimental results. In contrast, Gaussian noise augmentation only introduces random perturbations around the original samples and therefore cannot sufficiently capture the inherent correlations among acoustic features, resulting in larger prediction errors in several frequency bands. Furthermore, Table 7 summarizes the quantitative prediction error metrics of the models trained with the two augmentation strategies. The results further demonstrate the superior prediction performance of the WGAN-based augmentation approach in terms of accuracy.

In summary, compared with simple random noise perturbation, the WGAN-based augmentation method can better capture the nonlinear latent distribution characteristics underlying vehicle aeroacoustic responses and generate more representative synthetic samples. This approach enables more effective data enrichment, thereby improving the generalization capability and robustness of the SE-Xception prediction model under small-sample conditions.

TABLE 7 Comparison of different data augmentation strategies.

Augmentation strategy	MAPE (%)	RMSE (dB)
Gaussian noise augmentation	8.67	2.81
WGAN-based augmentation	3.75	1.20

© Jifeng Wang, Penghu Li, Jie Yan, Liang Zhang, Hongwei Yi, Yuwei Deng, Haibo Huang

6. Conclusions

To address the challenge of achieving efficient and accurate aerodynamic noise evaluation during the early stage of vehicle development, this study proposes a data-driven prediction framework integrating WGAN and SE-Xception. First, a WGAN-based data augmentation strategy is developed to alleviate the limitation of insufficient training samples by learning the distribution characteristics of the original wind noise dataset and generating high-quality synthetic samples. Subsequently, the augmented dataset is employed to train the SE-Xception prediction model, which effectively captures the complex nonlinear relationship between vehicle design parameters, acoustic transfer characteristics, and interior wind noise responses.

The proposed framework was further evaluated using three independent SUV vehicles that were completely excluded from the model development process, including WGAN training and five-fold cross-validation. The model achieved MAPE values of 3.18%, 3.75%, and 3.26%, with corresponding RMSE values of 1.12 dB, 1.20 dB, and 1.19 dB for the three validation vehicles, respectively. These results demonstrate the strong generalization capability of the proposed framework toward unseen vehicle configurations under practical engineering conditions.

Furthermore, the influence of the generated sample size on prediction performance was systematically investigated by constructing augmented datasets with different scales. The results indicate that increasing the number of generated samples initially improves model

performance by enriching the diversity of the training distribution. Specifically, when the generated sample size increased from 50 to 300, the RMSE decreased from 1.88 dB to 1.19 dB, indicating enhanced prediction accuracy. However, further increasing the generated samples to 400 and 500 resulted in increased RMSE values of 1.57 dB and 1.82 dB, respectively. This phenomenon suggests that excessive synthetic samples may introduce distribution deviations or redundant information, limiting further performance improvement. Therefore, considering the balance between prediction accuracy and data distribution reliability, 300 generated samples were selected as the optimal augmentation strategy.

Although the proposed interior wind noise prediction framework based on WGAN augmentation and the SE-Xception network demonstrates promising prediction accuracy and generalization capability under limited sample conditions, several limitations remain.

First, this study mainly focuses on SUV models, and the current dataset only covers the SUV design space. Since different vehicle categories, such as sedans, MPVs, and commercial vehicles, exhibit differences in body dimensions, geometric characteristics, aerodynamic behaviors, and acoustic transmission paths, their wind noise generation mechanisms may vary accordingly. Therefore, future work should establish multi-category and multi-platform datasets and explore transfer learning or domain adaptation methods to improve cross-vehicle prediction capability.

Second, the proposed model is developed under a steady driving condition of 120 km/h. Vehicle speed can significantly influence external flow structures, turbulence characteristics, and aerodynamic noise excitation mechanisms, resulting in different wind noise responses under varying operating conditions. Thus, further studies should incorporate multi-speed datasets to enhance the model's adaptability across different driving scenarios. Advanced approaches, such as multi-task learning and transfer learning, could also be investigated to improve prediction performance under diverse operating conditions.

Finally, the proposed framework aims to provide rapid wind noise evaluation based on vehicle styling parameters during the conceptual design stage. Compared with conventional methods requiring detailed vehicle models, CFD/CAA simulations, or wind tunnel tests, it enables early stage assessment before complete vehicle modeling. However, validation within practical vehicle development workflows has not yet been fully performed. Future research should further investigate its application in engineering design iterations, wind noise optimization, and industrial deployment.

Conflict of Interest

The authors and SAE International declare that one of the authors of this article was on the editorial board of the journal. SAE warrants that confidentiality was maintained throughout the peer-review process, and no partiality was granted to the work. SAE further warrants that the editorial board member had no influence and did not take part in any type of decision-making or peer review.

Acknowledgements

The authors are grateful to the Science and Technology Project of Sichuan Province (2026YFHZ0230, 2025ZYDF094) and the National Natural Science Foundation of China (No. 51905408).

Declaration of AI-Assisted Technologies

The authors declare that no generative AI technologies were used in the preparation and writing of this article. In doing so, the authors take full responsibility for the authenticity and scientific integrity of this article.

Contact Information

Jifeng Wang, corresponding author
wjf2024200289@my.swjtu.edu.cn

Haibo Huang, corresponding author
huanghaibo214@swjtu.edu.cn

CRediT Author Statement

Jifeng Wang: Software, Visualization, Writing—original draft

Penghu Li: Formal analysis

Jie Yan: Investigation

Liang Zhang: Validation

Hongwei Yi: Validation

Yuwei Deng: Data curation

Haibo Huang: Conceptualization, Funding acquisition, Supervision

References

1. Deubel, C., Ernst, S., and Prokop, G., "Objective Evaluation Methods of Vehicle Ride Comfort—A Literature Review," *Journal of Sound and Vibration* 548 (2023): 117515, doi:https://doi.org/10.1016/j.jsv.2022.117515.

2. Yildiz, M., Özkan, A., and Yildiz, A., "Development of Sound Quality Indices for Vehicle Acoustic Comfort Based on the Correlation between Customer Perception and Objective NVH Measurements," *International Journal of Engine Research* 27, no. 3 (2026): 471-481, doi:https://doi.org/10.1177/14680874251377143.
3. Yang, M., Dai, P., Yin, Y., Wang, D. et al., "Predicting and Optimizing Pure Electric Vehicle Road Noise via a Locality-Sensitive Hashing Transformer and Interval Analysis," *ISA Transactions* 157 (2025): 556-572, doi:https://doi.org/10.1016/j.isatra.2024.11.059.
4. Ganesan, K. and Seok, S., "Numerical Simulation and Parametric Optimization of Engine/Powertrain Mounts: Identifying Key Design Variables to Reduce NVH Noise," *KSAE/SAE 2025 Powertrain, Energy & Lubricants Conference & Exhibition*, Busan, South Korea, June 22, 2025, https://doi.org/10.4271/2025-01-0251.
5. Fabra-Rodriguez, M., Abellán-López, D., Simón-Portillo, F.J., Campello-Vicente, H. et al., "Numerical Model for Vibro-Acoustics Analysis of Tyre-Road Noise Generation Caused by Speed Bumps," *Applied Acoustics* 216 (2024): 109830, doi:https://doi.org/10.1016/j.apacoust.2023.109830.
6. Zhang, Y., He, T., Wang, Y., Niu, J. et al., "Research on the Influence of Door and Window Sealing on Interior Wind Noise Based on Statistical Energy Analysis," *SAE Int. J. Veh. Dyn., Stab., and NVH* 9, no. 3 (2025): 423-437, doi:https://doi.org/10.4271/10-09-03-0026.
7. Hadjit, R., Weilnau, K., Engels, B., Martin, S. et al. "Tire Noise Synthesis from Test Stand Measurements and CAE Full Vehicle Model," *13th International Styrian Noise, Vibration & Harshness Congress: The European Automotive Noise Conference*, Graz, Austria, June 19, 2024, https://doi.org/10.4271/2024-01-2951.
8. Dai, R., Zhao, J., Zhao, W., Ding, W. et al., "Exploratory Study on Sound Quality Evaluation and Prediction for Engineering Machinery Cabins," *Measurement* 253 (2025): 117684, doi:https://doi.org/10.1016/j.measurement.2025.117684.
9. Zou, T., Fu, Y., and Cao, P., "Vehicle Aerodynamic Noise: A Systematic Review of Mechanisms, Simulation Methods, and Bio-Inspired Mitigation Strategies," *Biomimetics* 11, no. 2 (2026): 99, doi:https://doi.org/10.3390/biomimetics11020099.
10. Viswanathan, H. and Chode, K.K., "The Role of Forebody Topology on Aerodynamics and Aeroacoustics Characteristics of Squareback Vehicles Using Computational Aeroacoustics (CAA)," *Flow, Turbulence and Combustion* 112, no. 4 (2024): 1055-1081, doi:https://doi.org/10.1007/s10494-023-00523-1.
11. Tajima, A., Ikeda, J., Nakasato, K., Kamiwaki, T. et al., "Numerical Simulation of Fluctuating Wind Noise of a Vehicle in Reproduced On-Road Wind Condition," *SAE Int. J. Adv. & Curr. Prac. in Mobility* 7, no. 1 (2024): 240-253, doi:https://doi.org/10.4271/2024-01-2353.
12. Du, J., Yang, P., and Qu, N., "Study on the Sound Quality of the Electric Vehicle Powertrain under Acceleration Conditions," *Measurement* 239 (2025): 115414, doi:https://doi.org/10.1016/j.measurement.2024.115414.
13. Guleria, A., Novacek, J., Ihi, R., Fougere, N. et al., "Validation of Wind Noise for Class-8 Truck Using Lattice Boltzmann Method," *SAE Int. J. Commer. Veh.* 18, no. 3 (2025): 391-408, doi:https://doi.org/10.4271/02-18-03-0021.
14. Mahmood, A., Cockerill, T., de Boer, G., Voss, J. et al., "Heat Transfer Modeling and Optimal Thermal Management of Electric Vehicle Battery Systems," *Energies* 17, no. 18 (2024): 4575, doi:https://doi.org/10.3390/en17184575.
15. Higgins, J., Fougere, N., Sondak, D., Senthooran, S., et al., "Machine Learning-Based Prediction of Wind-Induced Interior Noise in Ground Vehicles," *WCX SAE World Congress Experience*, Detroit, Michigan, United States, April 14, 2026, https://doi.org/10.4271/2026-01-0599.
16. Shin, S.-H. and Hashimoto, T., "Effects of Seat-Floor Vibration and Visual Brightness on the Perceived Sound Quality of Car Interior Noise," *The Journal of the Acoustical Society of America* 158, no. 1 (2025): 495-503, doi:https://doi.org/10.1121/10.0037190.
17. Su, B., Wang, Q., and Song, F., "Effectiveness of Seat's Negative Stiffness Structure on Three Different Models of Vehicles," *SAE Int. J. Passeng. Veh. Syst.* 18, no. 2 (2025): 167-180, doi:https://doi.org/10.4271/15-18-02-0011.
18. Aiash, A. and Robusté, F., "Total Noise Level's Passive Impact on Traffic Crashes: A Potential Distraction Indicator," *International Journal of Environmental Studies* 81, no. 3 (2024): 1058-1070, doi:https://doi.org/10.1080/00207233.2023.2213131.
19. Huang, H., Huang, X., Ding, W., Yang, M. et al., "Uncertainty Optimization of Pure Electric Vehicle Interior Tire/Road Noise Comfort Based on Data-Driven," *Mechanical Systems and Signal Processing* 165 (2022): 108300, doi:https://doi.org/10.1016/j.ymssp.2021.108300.
20. Ji, J., Wang, C., Wang, L., and Fu, S., "A Recursive Approach for Aeroacoustic Phased Array Measurements in Wind Tunnels," *The Journal of the Acoustical Society of America* 150, no. 1 (2021): 417-427, doi:https://doi.org/10.1121/10.0005543.
21. Puhle, C., Meyer, A., and Döbler, D., "On Improving CLEAN-SC Maps in the Wind Tunnel," *13th International Styrian Noise, Vibration & Harshness Congress: The European Automotive Noise Conference*, Graz, Austria, June 19, 2024, https://doi.org/10.4271/2024-01-2936.
22. Staron, D., Riegel, M., Blumrich, R., and Wagner, A., "Aeroacoustic Vehicle Development Method Considering Realistic Wind Conditions," Paper presented at *the INTER-NOISE and NOISE-CON Congress and Conference Proceedings*, Grand Rapids, MI, 2023, https://doi.org/10.3397/NC_2023_01_1123.
23. Jamaluddin, N., Oettle, N., and Staron, D., "Experimental Investigation into Modulated Aeroacoustic Cabin Noise Arising from Unsteady Flow Conditions," *SAE Int. J. Adv. & Curr. Prac. in Mobility* 7, no. 6 (2025): 2925-2939, doi:https://doi.org/10.4271/2025-01-0029.

24. Zhang, H., Jia, Q., and Wang, Y., "Identification and Analysis of Aerodynamic Sound Sources on the External Surface of an SUV," *Noise & Vibration Conference & Exhibition*, Grand Rapids, Michigan, United States, May 12, 2025, https://doi.org/10.4271/2025-01-0033.
25. Tajima, A., Hirata, T., Ikeda, J., Kamiwaki, T., et al., "Elucidation of Flow Mechanisms Modulating Vehicle Wind Noise by Using Large-Scale CFD Simulation," *WCX SAE World Congress Experience*, Detroit, Michigan, United States, April 14, 2026, https://doi.org/10.4271/2026-01-0614.
26. Xiong, Z., Zhang, X., Liu, P., Li, B. et al., "Optimization of Window Glass Parameters on Vehicle Weight and Wind Noise," *SAE Int. J. Passeng. Veh. Syst.* 18, no. 3 (2025): 281-298, doi:https://doi.org/10.4271/15-18-03-0018.
27. Josefsson, E., Sebben, S., and Urquhart, M., "Characterisation of the Flow around Passenger Vehicle Wheels with Varying Tyre Profiles," *International Journal of Heat and Fluid Flow* 103 (2023): 109191, doi:https://doi.org/10.1016/j.ijheatfluidflow.2023.109191.
28. Nomani, M., Kandekar, A., Latane, S., Manoji, A. et al., "Airborne Noise Mitigation for Roof-Mounted Air-Conditioning Unit Using Simulation-Based Flow-Induced Noise Detection Approach," SAE Technical Paper Series, 2025, https://doi.org/10.4271/2025-01-5002.
29. Sharma, S., Pawar, S., Singh, R., and Kalamdani, S., "Aero-Acoustic Characterization of a Commercial Vehicle Configuration Using CFD," *SAENIS TTTMS Thermal Management Systems Conference*, Guwahati, India, November 6, 2025, https://doi.org/10.4271/2025-28-0429.
30. Alwadei, F. and Alwadei, A., "Orthodontic Correction of an Anterior Open Bite with Periodontally Compromised Upper Incisors Using Miniscrews," *Applied Sciences* 14, no. 2 (2024): 811, doi:https://doi.org/10.3390/app14020811.
31. Zhang, X., Savoie, M., Quinn, M.K., Parslew, B. et al., "Simulation of Flow around a Finite Rectangular Prism: Influence of Mesh, Model, and Subgrid Length Scale," *Entropy* 27, no. 1 (2025): 65, doi:https://doi.org/10.3390/e27010065.
32. Cheng, C., Liu, Z., Chen, W., Li, X. et al., "A Multi-channel Active Noise Control System Using Deep Learning-Based Method to Estimate Secondary Path and Normalized-Clustered Control Strategy for Vehicle Interior Engine Noise," *Applied Acoustics* 228 (2025): 110263, doi:https://doi.org/10.1016/j.apacoust.2024.110263.
33. Shi, L., Wang, K., Chen, K., Lu, J. et al., "Virtual Feedback Control of Interior Road Noise Based on Headrest Loudspeakers," *Applied Acoustics* 227 (2025): 110234, doi:https://doi.org/10.1016/j.apacoust.2024.110234.
34. Raissi, M., Perdikaris, P., and Karniadakis, G.E., "Physics-Informed Neural Networks: A Deep Learning Framework for Solving Forward and Inverse Problems Involving Nonlinear Partial Differential Equations," *Journal of Computational Physics* 378 (2019): 686-707, doi:https://doi.org/10.1016/j.jcp.2018.10.045.
35. Roznowicz, D., Stabile, G., Demo, N., Fransos, D. et al., "Large-Scale Graph-Machine-Learning Surrogate Models for 3D-Flowfield Prediction in External Aerodynamics," *Advanced Modeling and Simulation in Engineering Sciences* 11, no. 1 (2024): 6, doi:https://doi.org/10.1186/s40323-024-00259-1.
36. Wang, T., Liu, Z., Chen, W., Kang, J. et al., "Anomaly Identification and Correction of Multi-dimensional Operating Conditions for a Data-Driven Vehicle Noise and Vibration Platform Based on Fusion of Deep Learning Models," *Proceedings of the Institution of Mechanical Engineers, Part D: Journal of Automobile Engineering* (2025): 09544070251411340, doi:https://doi.org/10.1177/09544070251411340.
37. Liu, J., Zhou, L., Huang, Y., Chen, D. et al., "Research on the Growth Rate Forecast of Intelligent Configuration Demand for New Energy Vehicles Based on the Xception Model (2025-2027)," *Procedia Computer Science* 281 (2026): 1300-1309, doi:https://doi.org/10.1016/j.procs.2026.05.015.
38. Xiang, X., Yi, H., Hou, J., Peng, C. et al., "Uncertainty Optimization of Vibration Characteristics in Engineering Machinery Powertrain Mounting Systems Using Monte Carlo and Genetic Algorithms," *SAE Int. J. Veh. Dyn., Stab., and NVH* 10, no. 1 (2025): 109-128, doi:https://doi.org/10.4271/10-10-01-0006.
39. Xie, F., Fan, Q., Li, G., Wang, Y. et al., "Motor Fault Diagnosis Based on Convolutional Block Attention Module-Xception Lightweight Neural Network," *Entropy* 26, no. 9 (2024): 810, doi:https://doi.org/10.3390/e26090810.
40. Talreja, J., Aramvith, S., and Onoye, T., "XTNSR: Xception-Based Transformer Network for Single Image Super Resolution," *Complex & Intelligent Systems* 11, no. 2 (2025): 162, doi:https://doi.org/10.1007/s40747-024-01760-1.
41. Pu, Z., Niu, K., and Ghadimi, N., "Deep Intelligent Intrusion Recognition in IoT Systems by Optimizing Xception Networks Based on Modified Pelican Optimization," *International Journal of Computational Intelligence Systems* 19 (2026): 68, doi:https://doi.org/10.1007/s44196-025-01144-4.
42. Huang, H., Wang, Y., Wu, J., Ding, W. et al., "Prediction and Optimization of Pure Electric Vehicle Tire/Road Structure-Borne Noise Based on Knowledge Graph and Multi-task ResNet," *Expert Systems with Applications* 255 (2024): 124536, doi:https://doi.org/10.1016/j.eswa.2024.124536.
43. Liu, Y., Hu, Y., Cao, G., and Wang, J., "SENet: Super-Resolution Enhancement Network for Crowd Counting," *Pattern Recognition* 162 (2025): 111420, doi:https://doi.org/10.1016/j.patcog.2025.111420.
44. Yecchuri, S. and Vanambathina, S.D., "Sub-Convolutional U-Net with Transformer Attention Network for End-to-End Single-Channel Speech Enhancement," *EURASIP Journal on Audio, Speech, and Music Processing* 2024, no.

1 (2024): 8, doi:https://doi.org/10.1186/s13636-024-00331-z.

45. Yu, F., Huang, Y., Chen, G., Yang, X. et al., "Engine Misfire Fault Detection Based on the Channel Attention Convolutional Model," *Computers, Materials & Continua* 82, no. 1 (2025): 843-862, doi:https://doi.org/10.32604/cmc.2024.058051.
46. Dasgupta, S., Mason, J., Yuan, X., Odeyomi, O. et al., "Enhancing Deepfake Detection Using SE Block Attention with CNN," Paper presented at *the 2024 International Conference on Artificial Intelligence, Big Data, Computing and Data Communication Systems (icABCD)*, Port Louis, Mauritius, 2024, https://doi.org/10.1109/icABCD62167.2024.10645262.
47. Goodfellow, I., Pouget-Abadie, J., Mirza, M., Xu, B. et al., "Generative Adversarial Networks," *Communications of the ACM* 63, no. 11 (2020): 139-144, doi:https://doi.org/10.1145/3422622.
48. Nayak, A.A., Venugopala, P., and Ashwini, B., "A Systematic Review on Generative Adversarial Network (GAN): Challenges and Future Directions," *Archives of Computational Methods in Engineering* 31, no. 8 (2024): 4739-4772, doi:https://doi.org/10.1007/s11831-024-10119-1.
49. Mohanan, A., Gangadharan Santha, S., Padmanabha Rajeswari, P., Padathil Veerendrakumar, P. et al., "Anomaly Detection Using Convolutional Neural Network and Generative Adversarial Network," *WCX SAE World Congress Experience*, Detroit, Michigan, United States, April 18, 2023, https://doi.org/10.4271/2023-01-0590.
50. Apostolou, N.E., Balourdou, E.V., Mouratidou, M., Tsalera, E. et al., "Efficient and Secure GANs: A Survey on Privacy-Preserving and Resource-Aware Models," *Applied Sciences* 15, no. 20 (2025): 11207, doi:https://doi.org/10.3390/app152011207.
51. Gao, H., Xiong, X., Shen, H., Yang, Y. et al., "Small-Sample and Imbalanced Milling Chatter Detection: Improved GAN with Attention and Hybrid Deep Learning," *Sound & Vibration* 59, no. 3 (2025): 3502-3502, doi:https://doi.org/10.59400/sv3502.
52. Iqbal, K., Rafique, A., Qaisar, S., and Tabassum, M., "Advancements and Challenges in the Development of Generative Adversarial Network (GANs) for Deep Learning," *Discover Networks* 1, no. 1 (2025): 11, doi:https://doi.org/10.1007/s44354-025-00007-w.
53. Zhou, J., Zhang, Z., Jin, Z., Kong, X. et al., "Indirect Measurement of Bridge Surface Roughness Using Vibration Responses of a Two-Axle Moving Vehicle Based on Physics-Constrained Generative Adversarial Network," *Journal of Sound and Vibration* 595 (2025): 118763, doi:https://doi.org/10.1016/j.jsv.2024.118763.
54. Veiner, J., Alajaji, F., and Gharesifard, B., "A Unifying Generator Loss Function for Generative Adversarial Networks," *Entropy* 26, no. 4 (2024): 290, doi:https://doi.org/10.3390/e26040290.
55. Ricardo Souza, M., Haris, A., Rodrigues, L., Offner, G. et al., "The Use of an Artificial Neural Network for Assessing Tone Perception in Electric Powertrain Noise, Vibration and Harshness," *Meccanica* 59, no. 3 (2024): 433-459, doi:https://doi.org/10.1007/s11012-024-01753-x.
56. Zhu, C., Lin, W., Zhang, H., Cao, Y. et al., "Research on a Bearing Fault Diagnosis Method Based on an Improved Wasserstein Generative Adversarial Network," *Machines* 12, no. 8 (2024): 587, doi:https://doi.org/10.3390/machines12080587.
57. Bender, T., Hoff, P., and Kleemann, R., "The New BMW Climatic Testing Complex - The Energy and Environment Test Centre," *SAE 2011 World Congress & Exhibition*, Detroit, Michigan, United States, April 12, 2011, https://doi.org/10.4271/2011-01-0167.
58. Zhou, Y., Diaz, M.A., Marx, D., Marchiano, R. et al., "Localizing Aeroacoustic Sources in Complex Geometries: A Hybrid Method Coupling 3D Microphone Array and Time-Reversal," *Journal of Sound and Vibration* 584 (2024): 118452, doi:https://doi.org/10.1016/j.jsv.2024.118452.
59. Liu, X., Pan, D., Zhao, W., Yang, X. et al., "Research and Application of Contribution Rate of Acoustic Transfer Function in Vehicles," *2025 International Conference on Transportation Infrastructure and Engineering (ICTIE2025)*, Guilin, China, June 6, 2025, https://doi.org/10.4271/2025-99-0343.
60. Ruggeri, G., Bertolini, C., and Horak, J., "New System for the Measurement of Sound-Insertion Loss on Small Samples: A Comparison with ASTM-E2611 and ASTM E90 Test Procedures," *Noise & Vibration Conference & Exhibition*, Grand Rapids, Michigan, United States, May 12, 2025, https://doi.org/10.4271/2025-01-0116.
61. Greenacre, M., Groenen, P.J., Hastie, T., d'Enza, A.I. et al., "Principal Component Analysis," *Nature Reviews Methods Primers* 2, no. 1 (2022): 100, doi:https://doi.org/10.1038/s43586-022-00184-w.
62. Yau, K.-L.A., Chong, Y.-W., Fan, X., Nejati, F. et al., "Combinations of Generative Adversarial Network and Reinforcement Learning: A Survey," *Neurocomputing* 650 (2025): 130847, doi:https://doi.org/10.1016/j.neucom.2025.130847.

Appendix A

TABLE A.1 Table of styling parameters.

Geometric parameter index	Geometric parameter detailed
Geometric parameter 1	Upper A-pillar X-axis dimension
Geometric parameter 2	Upper A-pillar Y-axis dimension
Geometric parameter 3	Front windshield upper radius
Geometric parameter 4	Lower A-pillar X-axis dimension
Geometric parameter 5	Lower A-pillar Y-axis dimension
Geometric parameter 6	Front windshield lower radius
Geometric parameter 7	Side mirror X-axis dimension
Geometric parameter 8	Side mirror Y-axis dimension
Geometric parameter 9	Side mirror Z-axis dimension
Geometric parameter 10	Side mirror leading edge angle
Geometric parameter 11	Side mirror trailing edge angle
Geometric parameter 12	Angle of the side mirror trailing edge parallel section
Geometric parameter 13	Length of the side mirror trailing edge parallel section
Geometric parameter 14	Side mirror to vehicle body distance
Geometric parameter 15	Roof deflection
Geometric parameter 16	Roof X-axis dimension
Geometric parameter 17	Rear windshield angle
Geometric parameter 18	Effective rear windshield angle
Geometric parameter 19	Front windshield rake angle
Geometric parameter 20	Hood inclination angle
Geometric parameter 21	Front grille angle
Geometric parameter 22	Approach angle
Geometric parameter 23	Departure angle
Geometric parameter 24	Frontal area
Geometric parameter 25	Side window inclination angle
Geometric parameter 26	Spatial angle between A-pillar and X-axis
Geometric parameter 27	Spatial angle between A-pillar and Y-axis
Geometric parameter 28	Spatial angle between A-pillar and Z-axis
Geometric parameter 29	Ground clearance
Geometric parameter 30–46	Vehicle acoustic transfer function

© Jifeng Wang, Penghu Li, Jie Yan, Liang Zhang, Hongwei Yi, Yuwei Deng, Haibo Huang

© 2027 Jifeng Wang, Penghu Li, Jie Yan, Liang Zhang, Hongwei Yi, Yuwei Deng, Haibo Huang. Published by SAE International. This Open Access article is published under the terms of the Creative Commons Attribution License (http://creativecommons.org/licenses/by/4.0/), which permits distribution, and reproduction in any medium, provided that the original author(s) and the source are credited.

Positions and opinions advanced in this work are those of the author(s) and not necessarily those of SAE International. Responsibility for the content of the work lies solely with the author(s).